

Computer Generation of Disordered Networks with Targeted Structural Properties

Florin Hemmann^{1,2,*}, Vincent Glauser^{1,3}, Ullrich Steiner^{1,2}, Matthias Saba^{1,2,†}

¹Adolphe Merkle Institute, University of Fribourg, Chemin des Verdiers 4, 1700 Fribourg, Switzerland

²NCCR Bio-inspired Materials, University of Fribourg, Chemin des Verdiers 4, 1700 Fribourg, Switzerland

³Department of Physics, University of Fribourg, Chemin du Musée 3, 1700 Fribourg, Switzerland

Abstract

Disordered spatial networks are model systems that describe structures and interactions across multiple length scales. Scattering and interference of waves in these networks can give rise to structural phase transitions, localization, diffusion, and band gaps. The study of these complex phenomena requires efficient numerical methods to computer-generate disordered networks with targeted structural properties. In the established Wooten-Weaire-Winer algorithm, a series of bond switch moves introduces disorder into an initial network. Conventional strain energies that govern this evolution are limited to 3D networks with coordination numbers of no more than four. We extend the algorithm to arbitrary coordination number statistics by introducing bond repulsion in the Keating strain energy. We tune the degree and type of disorder introduced into initially crystalline networks by varying the bond-bending force constant in the strain energy and the temperature profile. The effects of these variables are analyzed using a list of order metrics that capture both direct and reciprocal space. A feedforward neural network is trained to predict the structural characteristics from the algorithm inputs, enabling targeted network generation. As a case study, we statistically reproduce four disordered biophotonic networks exhibiting structural color. This work presents a versatile method for generating disordered networks with tailored structural properties. It will enable new insights into structure-property relations, such as photonic band gaps in disordered networks.

*florin.hemmann@unifr.ch

†matthias.saba@unifr.ch

1 Introduction

The analysis of disordered spatial networks is an active field of research in the natural and social sciences. Studied systems span a wide range of lengths and timescales and include atomic [1], polymeric [2], photonic [3], brain [4], geological [5], geographical [6], social [7], and economic systems [8]. Investigating their topology, spatial correlations, and temporal correlations is crucial for understanding fundamental phenomena such as phase transitions, localization, and transport. Examples of these phenomena at the microscopic level include the glass transition in molecular liquids and colloidal systems [9, 10], ionic transport in amorphous solid-state batteries [11, 12], and the localization of light and photonic band gap materials [13, 14].

Due to their statistical nature and complexity, numerical methods are essential for generating and analyzing disordered networks. Among these methods, Monte Carlo algorithms play a crucial role due to their inherently random nature, versatility, and computational efficiency [15]. The Wooten-Weaire-Winer (WWW) algorithm is a well-established Monte Carlo method for computer-generating continuous random networks – that is, disordered networks with a fixed coordination number [16, 17]. The WWW algorithm introduces disorder into an initial network by switching bond chains, relaxing introduced local strain by translating vertices, and accepting the state with the Metropolis acceptance probability, thereby lifting the system out of metastable states.

The WWW algorithm was introduced to model the structural correlations of amorphous semiconductors [16]. Following the original study, efforts were made to accelerate network generation by parallelizing the process, optimizing the annealing procedure, and rejecting unpromising bond switches early on [18, 19]. These advances have enabled the analysis of the melting transition of 2D continuous random networks [20], the crystallization of an initially amorphous silicon model [21], and the correct sampling of the Boltzmann distribution at finite temperatures [22].

The temperature profile affects network evolution via the Metropolis acceptance probability and is tailored to the networks under study. Previous work has focused on generating networks with minimal local strain to reproduce the experimental diffraction data of amorphous semiconductors [16, 18, 19, 23–25]. The temperature profile typically includes alternating periods of heating to a high, constant temperature (T) and quenching to $T = 0$, followed by annealing with gradually decreasing T . The resulting low-strain networks exhibit full electronic and photonic band gaps [13, 19]. A second class of studies has investigated the phase transition between the crystalline and amorphous states by observing a phase interface at a constant temperature or by gradually increasing the temperature [20–22, 26, 27].

The WWW algorithm includes additional degrees of freedom, such as the initial network and the functional form of the strain energy. These are linked through the coordination number statistic of the network. Early studies on this method involved randomizing four-valent 3D crystalline cubic diamond networks through a series of bond switches at high temperatures [16, 18, 23]. Later studies bypassed this randomization by starting with a random, homogeneously four-valent 3D configuration that remained within the framework of continuous random networks [19, 21, 24]. Conventional choices for the strain energy include the Keating energy [28] and the Stillinger-Weber potential [29]. Both contain two-body bond-stretching terms with equilibrium lengths and three-body bond-bending terms with equilibrium angles.

In three dimensions, networks with valencies of up to four are exceptional cases, in which all bonds in the ground state possess the same equilibrium angle. The same applies to 2D networks with coordination numbers up to three. However, for higher or mixed coordination numbers, strain potentials with fixed equilibrium angles generally do not favor bonds that uniformly cover the sphere. Tu *et al.* [26] modeled 3D silica with mixed valencies of 2 and 4 by setting the equilibrium angles to 180° for two-valent vertices and 109.5° for four-valent vertices. Bayley *et*

al. [30] extended this approach to arbitrary coordination numbers in 2D biological networks by setting the vertex-dependent equilibrium angle to $360^\circ/Z_i$, where Z_i is the valency of vertex i . In three dimensions, however, this method generally does not yield isotropic bond arrangements and is therefore not favorable. Thus, this limitation restricts the WWW algorithm to networks with coordination numbers of four or less.

Here, we overcome the limitations of the strain potentials used previously by setting the equilibrium angle to 180° for all vertices in the Keating energy. This yields angle-dependent repulsion. Since this angle can only be achieved by two-valent vertices, the bond angle energy generally increases compared to the equilibrium angles used previously. To compensate, we adjust the ratio of bond stretching to bond-bending energies in the Keating energy by modifying the bond-bending force constant β . We analyzed the effect of β under the new equilibrium angle by evolving six different crystalline networks with valencies up to eight. We selected the diamond [16] and gyroid [31] networks because the WWW algorithm has previously been applied to them, albeit with different equilibrium angles. The other four networks are less well-known and have never been investigated using WWW evolution.

We adjust the level of disorder in the melted networks by altering their temperature profiles during the transition from the crystalline state. We use a triangular heating and cooling sequence with adjustable temperature gradient and maximum temperature, followed by a quench. Using a list of 42 order metrics, we measure the effects of the initial network, the bond-bending force constant β , and the temperature profile parameters on the resulting networks. Specifically, we measure network primitive similarity by comparing bonds and angles, quantify homogeneity and isotropy in direct and reciprocal spaces, and characterize the network topology by determining coordination numbers and ring statistics. We trained a feedforward neural network to predict the order metric values as a function of the algorithm's input parameters for one of the initial crystalline networks, the three- and four-valent **ctn** network [32].

We demonstrate the capabilities of our extended WWW algorithm by statistically reproducing disordered biophotonic networks. These photonic materials exhibit structural color in nature at low refractive index contrasts and without long-range order [31, 33–37]. Computational studies of these networks are essential for elucidating the relationship between their structural characteristics and color. Using a dataset of thousands of generated networks, we identified networks with the highest similarity to three biological structures, as determined by our list of order metrics. There is good agreement between generated and biological networks, particularly with regard to small-length-scale order metrics, which are directly controlled by the Keating strain energy.

The article is organized as follows: Section 2 introduces the well-established WWW algorithm and its generalization to arbitrary coordination numbers and disorder control via the temperature profile. Then, Section 3 discusses the various order metrics to characterize the generated networks. Section 4 presents a case study outlining the computer-generated networks resembling biophotonic structures. After introducing the biological and initial networks for the extended WWW algorithm in Section 4.1, we examine how algorithm inputs affect generated networks in Section 4.2. Section 4.3 uses a neural network to predict the structural characteristics from algorithm inputs and evaluates its accuracy to investigate the statistical variance of the WWW algorithm. Section 4.4 identifies networks from the database that resemble biological structures and compares their order metrics.

2 Disordered network generation

The Wooten-Weaire-Winer (WWW) algorithm is a well-established Monte Carlo method for generating *continuous random networks*. These networks are disordered with *fixed valency*, meaning all vertices have the same coordination number Z [16]. First, we will discuss the original method used to produce disordered networks resembling amorphous semiconductors. Next, we will introduce our extensions that handle networks with *varying valency*, where multiple coordination numbers are present. Lastly, we will explain how adjusting WWW algorithm parameters can alter the degree of disorder.

2.1 Established Wooten-Weaire-Winer algorithm

This algorithm introduces disorder into an initial configuration by performing a series of bond switches that leave the coordination numbers invariant but alter the network's overall topology.

The initial network configuration may be crystalline [16] or amorphous [19]. The WWW algorithm is typically applied to networks with 10^3 to 10^4 vertices and periodic boundary conditions, which are used throughout this article. Most of the literature focuses on networks with valency $Z = 4$. The initial network is therefore either the cubic diamond network **dia** [16]¹ or a disordered network with fixed $Z = 4$. We define a strain energy for this initial network. A common choice is the Keating energy for networks with $Z = 4$ [28],

$$\mathcal{E} = \frac{3}{16} \frac{A}{d^2} \sum_{\langle ij \rangle} (\mathbf{R}_{ij} \cdot \mathbf{R}_{ij} - d^2)^2 + \frac{3}{8} \frac{B}{d^2} \sum_{\langle jik \rangle} \left(\mathbf{R}_{ij} \cdot \mathbf{R}_{ik} + \frac{1}{3} d^2 \right)^2 . \quad (1)$$

Here, d is the strain-free equilibrium bond length, i , j , and k are labels for the vertices. The bond connecting vertices i and j is $\mathbf{R}_{ij} = \mathbf{R}_j - \mathbf{R}_i$. Summation over all neighboring vertices i and j is denoted by $\sum_{\langle ij \rangle}$, and summation over all connected vertex chains $j - i - k$ is denoted by $\sum_{\langle jik \rangle}$. Furthermore, A and B are the force constants for stretching and bending bonds, respectively. We define the corresponding dimensionless Keating energy, length, and force weight,

$$E = \frac{\mathcal{E}}{Ad^2} , \quad \mathbf{r}_{ij} = \frac{\mathbf{R}_{ij}}{d} , \quad \beta = \frac{B}{A} .$$

Thus, the non-dimensionalized form of (1) becomes

$$E = \frac{3}{16} \sum_{\langle ij \rangle} (r_{ij}^2 - 1)^2 + \frac{3}{8} \beta \sum_{\langle jik \rangle} \left(\mathbf{r}_{ij} \cdot \mathbf{r}_{ik} + \frac{1}{3} \right)^2 = E_r + E_\theta^{\text{orig}} . \quad (2)$$

The original network configuration has a total strain energy E_i . This configuration is modified by randomly reconnecting a chain of bonds, as illustrated in Figure 1. This *bond switch* preserves the coordination numbers. Thus, the initial configuration defines the coordination number statistics and correlations. However, the bond switch introduces local strain into the network. This strain is relaxed iteratively by successively moving the vertices, starting from the switched chain and moving outward to higher neighbor shells [18]. Each vertex is translated to a position of minimal stress, which is approximated using the strain energy gradient as described in ref. [39]. The local relaxation of all vertices marks the completion of one *relaxation cycle*. This cycle is repeated approximately 25 times to reach *relaxation* or convergence toward the true equilibrium positions of all vertices. The new network configuration, which has a total strain energy of E_f , is accepted using the Metropolis acceptance probability [40]

$$P_{\text{accept}} = \min \left[1, \exp \left(\frac{\mathcal{E}_f - \mathcal{E}_i}{k_B T} \right) \right] = \min \left[1, \exp \left(\frac{E_f - E_i}{T} \right) \right] . \quad (3)$$

¹For all network structures, we use the nomenclature of the Reticular Chemistry Structure Resource [38].

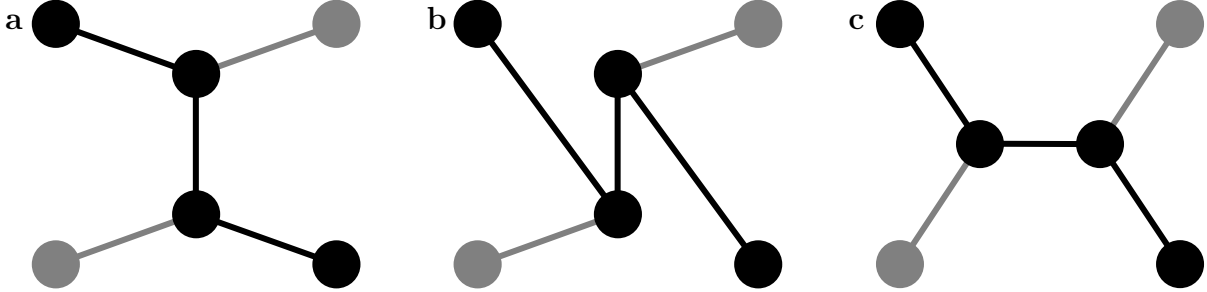


Figure 1: A Monte Carlo move is shown for a 2D, three-valent network. **a** A chain of four vertices (black) is randomly selected. **b** A bond switch reconnects the vertices while maintaining all coordination numbers. **c** The stress introduced by the bond switch is relaxed by translating the vertices.

Here, \mathcal{T} is the physical temperature, and $T = \frac{k_B \mathcal{T}}{Ad^2}$ is the dimensionless temperature. A *Monte Carlo move* involves random bond switching, relaxation, and acceptance or rejection.

We use one *Monte Carlo step* as the unit of simulation time. A step is finished when an attempt to switch a bond is made on average on every available bond chain. The number of available bond chains is estimated based on the number of vertices N_{vertices} and the mean coordination number \bar{Z} . There are N_{vertices} choices for the first vertex of the chain, \bar{Z} for the second vertex connected to the first, and $\bar{Z} - 1$ choices for the third and fourth vertices, respectively. Since the order of the chain is irrelevant, we divide by two to obtain the number of chains [19]

$$N_{\text{chains}} = N_{\text{vertices}} \cdot \bar{Z} \cdot (\bar{Z} - 1)^2 / 2 .$$

In Ref. [19], the WWW algorithm is accelerated by using a local/nonlocal relaxation procedure. Before performing a relaxation, a threshold energy

$$E_t = E_i - T \ln(s)$$

with random $s \in (0, 1]$ is set. After the bond switch, only the three innermost neighbor shells are relaxed for the first ten relaxation cycles. If it becomes clear during local relaxation that the final energy E_f will not fall below the threshold energy E_t , the bond switch is rejected early. To estimate E_f during local relaxation, we use the fact that the energy is harmonic around the minimum and can be expressed as a function of force F and a proportionality constant c_f :

$$E_f \approx E - c_f |F|^2 .$$

Fitting this equation to the total energy and strain force of the last two relaxation cycles yields E_f and c_f . If $E_f > E_t$ during local relaxation, the bond switch is rejected. To account for anharmonicities, no moves are rejected during the first five relaxation cycles. After ten cycles, relaxation continues globally without early rejections, as in the original WWW algorithm.

A nearly fully local relaxation scheme is introduced in Ref. [24], wherein global relaxation only occurs if E_f is slightly above E_t . This allows for the formation of large networks with up to 20,000 vertices. While global relaxation can reduce stress in a locally relaxed network, it introduces dependence on system size in the change of total strain energy. Therefore, network evolution depends on both temperature and the number of vertices. Since our goal is to achieve evolution independent of system size, we use an entirely local relaxation scheme, which results in slightly higher strain.

2.2 Extension to networks with arbitrary valency

We modify the Keating energy [28] to generate networks with any desired coordination number statistic. This is necessary when modeling arbitrary 3D disordered networks. To our knowledge,

the WWW algorithm has only been used for 3D systems with coordination numbers of four or fewer [16, 19, 23–26, 31]. Reported networks with higher coordination numbers are two-dimensional only [30]. Furthermore, when evolving networks with varying valency, the bond bending energy in Equation (2) depends on coordination [25, 26, 30, 41]. These limitations stem from the equilibrium angle of the Keating strain energy.

To relax a network with arbitrary coordination numbers, the bond bending term E_θ^{orig} must be modified in the Keating energy in Equation (2). Since the equilibrium angle is typically set to a value corresponding to the coordination number, this term requires adjustment. In the above example, the equilibrium angle for diamond-like networks with $Z=4$ is $\theta_{\text{eqm}} = \arccos(-1/3) \approx 109.5^\circ$, resulting in

$$E_\theta^{\text{orig}} \sim \left(\mathbf{r}_{ij} \cdot \mathbf{r}_{ik} + \frac{1}{3} \right)^2 = \left(r_{ij} r_{ik} \cos(\theta_{jik}) + \frac{1}{3} \right)^2 \stackrel{!}{=} 0 \quad (4)$$

$$\Rightarrow r_{ij} = r_{ik} = d \quad \text{and} \quad \theta_{jik} = \theta_{\text{eqm}} = \arccos\left(-\frac{1}{3}\right) \quad . \quad (5)$$

The equilibrium angle is the angle between all bonds in the 4-valent cubic diamond network **dia**, with $\theta_{\text{dia}} = \theta_{\text{eqm}} = \arccos(-\frac{1}{3})$ [42]. Another crystallographic network in which all bonds span the same angle is the 3-valent gyroid network **srs**, with $\theta_{\text{eqm}} = \theta_{\text{srs}} = 120^\circ$. Therefore, analogously to **dia**, the **srs** is the ground state of the Keating energy with appropriately chosen equilibrium angle. However, this strategy fails for networks with mixed coordination numbers, where each vertex requires an individual equilibrium angle [26, 30, 41]. There is no configuration with a single bond angle for vertices with valency $Z > 4$, which are present in many other networks [1, 2, 4–8, 30]. Consequently, there is no value of θ_{eqm} that yields a vanishing ground state bond bending energy $E_\theta^{\text{orig}} = 0$.

To generate disordered networks with arbitrary valency, the bond bending term E_θ^{orig} in the Keating energy (Equation (2)) must be modified. To favor bonds that uniformly cover the sphere for any coordination number, we propose bonds that energetically repel each other. Here, *sphere* refers to the idealized surface surrounding the vertex, on which the bond directions are arranged as evenly as possible. This is achieved by setting the equilibrium angle to $\theta_{\text{eqm}} = 180^\circ$, regardless of the coordination number. Thus, the lowest bending energy at a given vertex is positive. For a small coordination number ($Z=3$ and 4), the energy is minimized by the well-known **srs** (equilateral triangle) and **dia** (regular tetrahedron) bonds. For larger $Z < 10$, the energy is minimized by the solutions to Feje's problem [43], which maximizes the distance between points on a sphere. The energy is also minimized by connecting the center to the vertices of Platonic solids.² Thus, we propose the following generalized Keating energy, which favors uniformly covering the unit sphere with bond angles for arbitrary valency,

$$E = \frac{3}{16} \sum_{\langle ij \rangle} (r_{ij}^2 - 1)^2 + \frac{3}{8} \beta \sum_{\langle jik \rangle} (r_{ij} r_{ik} \cos(\theta_{jik}) + 1)^2 = E_r + E_\theta \quad . \quad (6)$$

For vertices with a valency $Z > 2$, there is no bond arrangement in which all angles are $\theta_{\text{eqm}} = 180^\circ$. Therefore, for four-connected networks, $E_\theta > E_\theta^{\text{orig}}$, increasing monotonically with Z . One method to counteract the increase in angle energy is to vary the bond bending force constant β , which sets the ratio of bond bending to bond stretching energy. In this work, we use a global β to control the relative degrees of disorder in bond lengths and angles. For polyvalent

²However, for $Z > 5$, a higher-dimensional manifold of minimum energy can be found in the configuration space. For example, when $Z=6$, the regular octahedron can transform into a triangular antiprism with an arbitrary torsion angle in the [111] direction while remaining within the global energy minimum. When $Z=8$, the cube (a Platonic solid corresponding to a **bcu** network [38], or an IWP minimal surface structure [36]) and the quadratic antiprism (Feje's solution) lie on a similar torsion-degenerate line of minimum energy in configuration space.

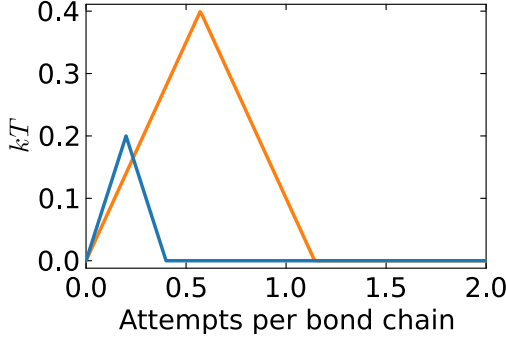


Figure 2: In our extended WWW algorithm, we introduce disorder to networks by successively heating, cooling, and quenching them. The quench continues until it is no longer possible to reduce the strain energy through additional Monte Carlo moves.

networks, one could introduce a valency-dependent β to accommodate the Z -dependence of energy and expand the range of accessible disordered network morphologies.

2.3 Heating profile and melting temperature

In addition to the bond-bending constant β , the degree of disorder in the generated networks can be adjusted by altering the temperature profile during network evolution. We found that the triangular profile shown in Figure 2 provides reasonable control over the structural properties of the resulting networks. This profile consists of constant heating with gradient ΔT up to maximum temperature T_{\max} , followed by constant cooling with gradient $-\Delta T$ down to $T=0$, concluding with a quench. Evolution occurs at $T=0$ until no single bond switch can decrease the total strain energy. This temperature profile has two degrees of freedom: ΔT and T_{\max} . These can be used to adjust the degree of disorder introduced into the initial network.

When a low-strain initial network is heated, bond switches are only likely to be accepted once the *melting temperature* T_{melt} is reached. We define T_{melt} as the temperature at which the energetically lowest bond switch and relaxation are accepted with probability $P_{\text{accept}} > P_{\text{melt}} := 0.1\%$. This causes the initial periodic configuration to begin melting. Isolating T in the Metropolis acceptance probability in Equation (3) yields the melting temperature

$$T_{\text{melt}} = \frac{E_f - E_i}{\ln(P_{\text{melt}})} \quad . \quad (7)$$

Due to the Boltzmann distribution in P_{accept} , Monte Carlo moves can be accepted at any finite temperature $T > 0$, including temperatures below T_{melt} . However, T_{melt} serves as an estimate when melting is likely to occur and as a reference for rescaling temperatures when changing the bond-bending force constant β or the equilibrium angle θ_{eqm} .

Section 4 discusses how variations of β and the temperature profiles affect the degree of disorder in the generated networks. The next section introduces the metrics used to quantify structural disorder.

3 Order metrics

Network structure disorder can be quantified in various ways. These aspects fall into four main categories, which are discussed in detail below: Similarity of primitives, homogeneity, isotropy, and topological classification.

3.1 Similarity of network primitives

A variety of short-range order metrics are suitable for measuring the similarity of the network primitives consisting of multiple bonds that meet at a vertex. We calculate the standard deviations of the bond length and bond angle, σ_r and σ_θ , respectively. Additionally, we determine the mean value \bar{q}_l and standard deviation σ_{q_l} of the Steinhardt local bond order parameters q_l for all vertices [44]. We compute the parameters to order $l \leq 12$ because higher orders do not provide meaningful information for coordination numbers $Z \lesssim 10$.

Additionally, we determine the order of neighboring primitive orientations by computing the distribution of dihedral angles. For all chains of four connected vertices $j - i - k - l$, we consider the dihedral angles between the planes spanned by \mathbf{r}_{ij} and \mathbf{r}_{jk} , and by \mathbf{r}_{jk} and \mathbf{r}_{kl} [45],

$$\phi_m = \text{atan2} \left(\mathbf{r}_{jk} \cdot ((\mathbf{r}_{ij} \times \mathbf{r}_{jk}) \times (\mathbf{r}_{jk} \times \mathbf{r}_{kl})), |\mathbf{r}_{jk}|((\mathbf{r}_{ij} \times \mathbf{r}_{jk}) \cdot (\mathbf{r}_{jk} \times \mathbf{r}_{kl})) \right) \quad .$$

The index m labels all four-vertex chains, and atan2 is the two-argument arctangent function. Since the dihedral angle distribution usually has multiple peaks, we create an 18-bin ($N_{\text{bins}} = 18$) histogram $p(\phi_m)$, with 10° bin widths and centers ϕ_m . We then determine the normalized information entropy of the resulting distribution, called *dihedral angle entropy*,³

$$h_\phi = -\frac{1}{\log(N_{\text{bins}})} \sum_{i=1}^{N_{\text{bins}}} p(\phi_m) \log(p(\phi_m)) \quad .$$

3.2 Homogeneity

To extend the order quantification beyond individual primitives, we analyze the statistical homogeneity of the network by examining the interparticle distances. For statistically isotropic and homogeneous materials, the dimensionless pair correlation function $g_2(r)$ represents the mean particle density at distance r from a reference particle divided by the total mean particle density, $g_2(r) = n(r)/n_0$ [42]. Another commonly used function to describe particle densities is the three-dimensional radial distribution function, defined as the mean number of particles per unit length, $\rho(r) = 4\pi r^2 n_0 g_2(r)$. The cumulative coordination number $Z(r) = \int_0^r dr' \rho(r')$ is the expected number of particles within a sphere of radius r centered at a reference particle [47]. We define the *coordinated neighbor distance* r_c as the radius at which $Z(r_c) = 1$. $r_c = 1$ indicates a homogeneous network whereas $r_c \lesssim 0.7$ may indicate vertex clustering.

Since r_c only captures distances between connected vertices, we use r_u , *uncoordinated neighbor distance*, as an additional measure of network homogeneity. r_u is the average distance from vertex i to the closest unconnected vertex j . Unlike connected vertices, it is not included in the bond stretching term of the Keating energy (Equation (6)). Therefore, we expect less control over r_u via the tuning knobs of the extended WWW algorithm. r_u is obtained by calculating the pair correlation function $g_2^u(r)$, the radial distribution function $\rho_u(r)$, and the cumulative coordination number $Z_u(r)$. This calculation takes into account only vertex pairs that are not connected by a bond. r_u is defined as the distance at which $Z_u(r_u) = 1$. Vertex clustering may occur when $r_u \lesssim 1$.

³ h_ϕ is a simple measure of uniformity in the dihedral angle distribution. The contribution of dihedral angles to the thermodynamic entropy of networks and chains is studied in [46].

Furthermore, the statistical homogeneity of a network can be quantified by calculating the geometrical pore size distribution $P(r)$ [48]. $P(r)$ represents the typical size scale(s) of the void space, that is, the volume of the network excluding its vertices and infinitely thin bonds. The pore size distribution is linked to the fraction of the void space accessible to a sphere of radius r without bond overlap via the integral $V(r) = \int_0^r dr' P(r')$. We use the algorithm developed by Song et al. [49] to determine $P(r)$ numerically and sample points on a 3D grid with a grid size of $0.2d$. For each grid, we determine the radius of the largest sphere that contains the grid point and does not intersect the mathematical network. $P(r)$ is the histogram of these sphere radii. The *critical pore radius* δ_c is the maximum radius of a sphere that can percolate through the void space [50]. It can be accurately estimated using the second moment of the pore size distribution [50],⁴

$$\delta_c \approx \left(\int_0^\infty dr r^2 P(r) \right)^{\frac{1}{2}} .$$

A critical pore radius $\delta_c \gtrsim 0.5$ indicates the presence of large pores, which can result from vertex clustering.

Additionally, information from reciprocal space can be used to determine the homogeneity of a structure at large length scales. This concept is related to hyperuniformity [47, 53]. As before, we use dimensionless units where positions are given in units of d , and wave vectors and wave numbers are scaled by $1/d$. A hyperuniform system is characterized by a vanishing structure factor in the limit of infinitely small wave vectors [53],

$$\lim_{\mathbf{k} \rightarrow 0} S(\mathbf{k}) = 0 . \quad (8)$$

In direct space, this property translates to a suppression of large-length-scale density fluctuations [47]. When testing the hyperuniformity criterion of Equation (8) for finite-size systems, the structure factor must be extrapolated to $\mathbf{k} \rightarrow 0$ since the minimal wave number $k_{\min} \equiv |\mathbf{k}|_{\min}$ depends on the system size. For a system with edge length L and periodic boundary conditions, the largest length scale is $L/2$, and the smallest feasible wave number is $k_{\min} = 4\pi/L$.

We calculate two types of structure factors. First, we consider only the point cloud of vertices at positions \mathbf{x}_i and use the scattering intensity estimator [54]

$$S_v(\mathbf{k}) = \frac{1}{N_v} \left| \sum_{i=1}^{N_v} \exp(-i\mathbf{k} \cdot \mathbf{x}_i) \right|^2 . \quad (9)$$

Second, we consider infinitely thin bonds and obtain

$$S_b(\mathbf{k}) = \frac{1}{N_b} \left| \sum_{i=1}^{N_b} 2 \operatorname{sinc}(\mathbf{k} \cdot \mathbf{r}_i) \exp(-i\mathbf{k} \cdot \mathbf{x}_i) \right|^2 . \quad (10)$$

Here, \mathbf{x}_i is the position of the center of bond i , and \mathbf{r}_i is the vector connecting the endpoints (vertices). $S_b(\mathbf{k})$ provides more information about the network than $S_v(\mathbf{k})$ but comes at the cost of increased computational complexity.

To investigate the hyperuniformity of a network, we calculate the angle-average of the structure factor including bonds $S(k) \equiv \overline{S}_b(k)$ and write it in the limit of small wave numbers as [47]

$$\lim_{k \rightarrow 0} S(k) = k^\alpha . \quad (11)$$

⁴Note that Klatt et al. [50] use the definition of the pore size distribution of Torquato et al. [51], which differs from Gelb et al.'s [48] definition of $P(r)$ used in this article. The two definitions are compared in Agrawal et al. [52].

The exponent α serves as a *hyperuniformity metric*. By comparing Equations (8) and (11), we see that non-hyperuniform systems have an exponent of $\alpha \leq 0$. Hyperuniform systems have $\alpha > 0$ and are divided into three classes [47]. Class I systems possess $\alpha > 1$. This class contains all crystals, most quasicrystals, and some disordered systems. The two weaker hyperuniform classes are class II, with $\alpha = 1$, and class III with $0 < \alpha < 1$. A power law describes the decay in density fluctuations in classes I and III at large length scales. Class II is a special case in which fluctuations fall off logarithmically [47].

Excess spreadability is a robust method for extrapolating the scaling of the structure factor as k approaches zero and for determining the hyperuniformity metric α [55]. In a diffusion process involving a solute initially present in one phase but not in the other, the diffusion spreadability $\mathcal{S}(t)$ is the amount of solute in the initially empty phase over time. This assumes that both phases have the same diffusion constant D [56]. Using dimensionless units, time t is written in units of d^2/D . The excess spreadability $\mathcal{S}(t) - \mathcal{S}(\infty)$ at time t can be calculated using the structure factor including bonds (Equation (10)). In 3D, it takes the form [55]

$$\mathcal{S}(t) - \mathcal{S}(\infty) = \frac{1}{(2\pi)^3} \int_{\mathbb{R}^3} d\mathbf{k} S_b(\mathbf{k}) \exp(-k^2 t) . \quad (12)$$

For long times t , the excess spreadability scales as [55]

$$\lim_{t \rightarrow \infty} \mathcal{S}(t) - \mathcal{S}(\infty) \sim 1/t^{(3-\alpha)/2} . \quad (13)$$

Using Equation (12) to calculate the excess spreadability from the structure factor including bonds for various times t , the hyperuniformity metric α can thus be estimated by fitting Equation (13). To determine a feasible range of times for the fit, consider Equation (12) for the angle-averaged structure factor,

$$\mathcal{S}(t) - \mathcal{S}(\infty) = \frac{1}{2\pi^2} \int_0^\infty dk S(k) k^2 \exp(-k^2 t) . \quad (14)$$

For our system sizes, the structure factor can be calculated for wave numbers in the range $k \in [\pi/4, 4\pi]$. In Equation (14), this k -range is sampled by $t \in [0.1, 1]$. For this range of t , we estimate α by calculating the average slope of $\mathcal{S}(t) - \mathcal{S}(\infty)$ in a double-logarithmic plot. This robust method is effective for relatively small system sizes and does not require us to assume a functional form of the structure factor as k approaches zero.

3.3 Isotropy

We quantify the statistical isotropy of a network using information from direct and reciprocal spaces. First, we define a metric for direct space isotropy based on variation in bond orientations. When categorizing the network's bonds by their direction vectors \mathbf{b} , variance in bin counts indicates isotropy. We obtain forty orientation bins ($N_b = 40$) by subdividing each triangular face of a regular icosahedron into four equilateral triangles and consider only one hemisphere of the subdivided icosahedron. Each resulting bin covers a solid angle of $4\pi/80 = \pi/20$ and the centers of the bins are approximately 20.9° apart in direction \mathbf{b}_i . All network bonds are then assigned to their closest bin direction \mathbf{b}_i . We call the normalized information entropy of the bond orientation distribution $p(\mathbf{b}_i)$ *bond orientation entropy*,

$$h_b = -\frac{1}{\log(N_b)} \sum_{i=1}^{N_b} p(\mathbf{b}_i) \log(p(\mathbf{b}_i)) . \quad (15)$$

We find empirically that the values of $h_b \gtrsim 0.975$ correspond to statistically isotropic networks, while networks with smaller values of h_b exhibit crystalline domains.

A second class of isotropy metrics is obtained from information in reciprocal space using the structure factors given by Equations (9) and (10). Unlike anisotropic systems, such as crystals, which exhibit Bragg peaks, statistically isotropic structures have angle-independent structure factors. We quantify the angle dependence of the two structure factors $S_j(\mathbf{k})$, $j \in \{v, b\}$, by first averaging them over angles to obtain the means $\bar{S}_j(k)$ and standard deviations $\sigma_{S_j}(k)$. We then calculate the normalized *anisotropy metrics*

$$A_j = \frac{1}{N_l} \sum_{k_l} \frac{1}{\bar{S}_j(k_l)/\sigma_{S_j}(k_l) + 1} \quad (16)$$

for $N_l = 5$ wave numbers $k_l \in \{\pi, \frac{5\pi}{4}, \frac{3\pi}{2}, \frac{7\pi}{4}, 2\pi\}$. We add 1 to the denominator to normalize the metric to the range $A_j \in [0, 1]$. Anisotropic networks exhibit values of $A_j \gtrsim 0.6$. Generally, A_v and A_b are similar. For the remainder of the article, we will focus on the bond metric A_b because it contains information about the mathematical network that the vertex metric A_v does not.

3.4 Topology

We classify disordered networks based on their topological properties, such as coordination number and ring statistics. First, we calculate the mean \bar{Z} and standard deviation σ_Z of the coordination number distribution. These are inherited from the crystallographic starting networks because the WWW algorithm conserves coordination numbers. Next, we determine the ring size distribution by considering all very strong rings, that is, rings containing at least one bond that does not belong to a shorter ring [57]. The ring size s_i is the number of bonds in the ring i . Then, we calculate the mean ring size \bar{s} and its standard deviation σ_s from the ring size distribution.

To estimate the geometric ring sizes, we first project the 3D rings onto two-dimensional planes. We treat each ring as a polygon and use Newell's method to estimate the normal vector \mathbf{n} that maximizes the polygon's area when projected along \mathbf{n} [58]. Then, we project the polygon onto the plane defined by \mathbf{n} and determine its pole of inaccessibility. This point is maximally distant from all edges of the projected polygon. We call the minimum distance from the pole of inaccessibility to any edge of the projected ring *ring radius* r_s , as it estimates the radius of the largest circle that can fit inside the ring. We determine the ring radii of all very strong rings in the network and calculate their mean \bar{r}_s and standard deviation σ_{r_s} .

We have now introduced a comprehensive list of metrics that quantify disorder in network structures across different length scales. The list is summarized in Table 2, Appendix A. In the next section, we determine the parameter space of metrics that can be reached using the extended WWW algorithm introduced in Section 2. We also demonstrate how our network generation and characterization method can be used to statistically reproduce disordered biophotonic networks.

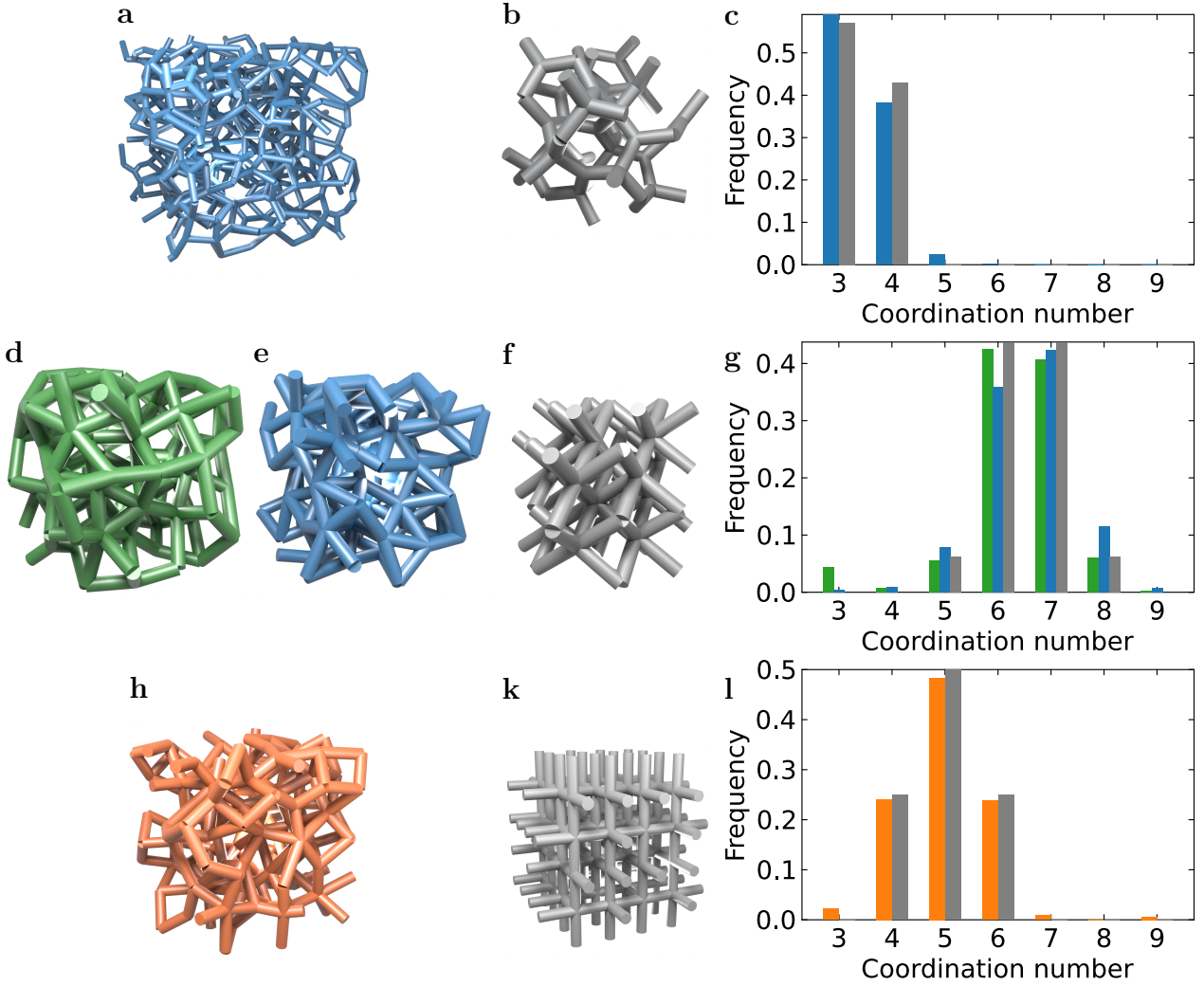


Figure 3: **a** A section of the skeletonized, disordered photonic network of the *Pachyrhynchus congestus mirabilis* weevil gives rise to blue structural color (PCM blue). **b** The periodic **ctn** network has similar coordination number statistics as PCM blue, as shown in **c**. **d** and **e** show sections of the StV green and StV blue biological networks, respectively. **f** The periodic **bcu_{mod}** network has coordination number statistics similar to those of StV green and StV blue, as shown in **g**. There Sta orange network in **h** and the periodic **pcu_{mod}** network in **k** have similar coordination number statistics, as shown in **l**.

4 Case study: reproducing biophotonic networks

In this section, we investigate how the parameters of the extended WWW algorithm (Section 2) impact generated networks. As a test scenario, we consider biophotonic networks that produce structural color. We statistically reproduce these networks using the order metric list from Section 3.

4.1 Disordered biophotonic and initial periodic networks

Structural color arises from the interference of visible light in the presence of biophotonic nanostructures in many animals and plants [35]. As dielectric contrast increases, these structures can form complete photonic band gaps (PBGs), which prevent light from entering at any angle [59]. This phenomenon is well-established in periodic systems, or photonic crystals. However, a thorough understanding of how a reduced photonic density of states emerges in disordered structures is still needed. Our goal is to statistically reproduce these disordered

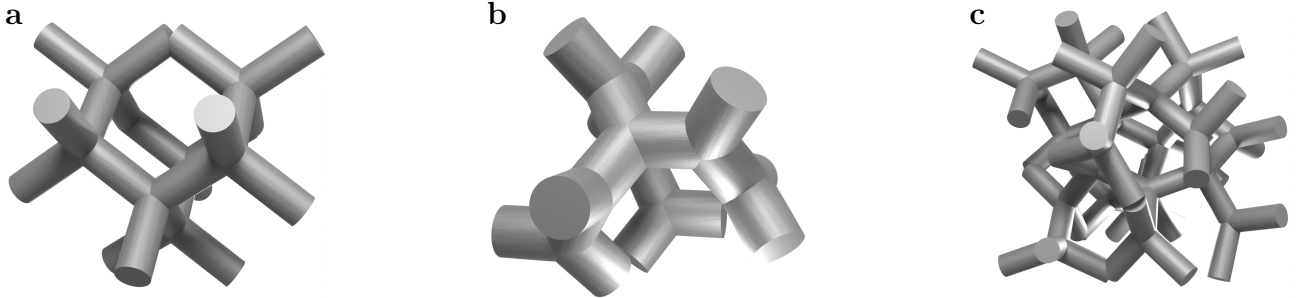


Figure 4: We applied the extended WWW algorithm to the periodic diamond **dia** (a), gyroid **dia** (b), and **lcs** (c) networks, which have wide photonic band gaps.

biophotonic networks, laying the groundwork for future work to explore how their structural characteristics affect the photonic density of states. To achieve this, we will use the extended WWW algorithm introduced in Section 2 and the order metrics from Section 3.

This study focuses on reproducing biophotonic networks based on existing 3D network data. This data was obtained using focused ion beam scanning electron microscopy (FIB-SEM). FIB-SEM tomography was performed, followed by image processing and skeletonization [34]. Djeghdi et al. analyzed the disordered photonic network in the wing scales of the *Pachyrhynchus congestus mirabilis* weevil, which exhibit blue structural color (PCM blue), using this method. Figure 3a illustrates a section of the skeletonized network. Bauernfeind et al. analyzed structurally colored wing scales in *Sternotomis virescens* (StV green and StV blue, Figures 3d and 3e) [36] and *Sternotomis amabilis* (StA orange, Figure 3h) [37] longhorn beetles using the same tomography approach.

As discussed in Section 2.1, the coordination number statistic of the final disordered network is determined by the initial network in both the original WWW algorithm and our extension. Therefore, we selected periodic initial networks from the crystallographic database [38] with coordination number distributions similar to those of the biological networks. To reproduce the PCM blue network, we started with the **ctn** network (Figure 3b) because both networks have coordination numbers $Z \approx 3.4 \pm 0.5$ (Figure 3c). Filtering the database [38] for cubic space groups with ≥ 195 and valencies $Z \in \{3, 4\}$ yields the **ctn** network as one with the least complex unit cell, i.e., the smallest genus.

As discussed by Bauernfeind et al. [36] and analyzed in more detail in Section 4.4, the StV green and StV blue networks (Figures 3d,e) have very similar order metrics. The color difference stems from the larger strut lengths of the green network, as evidenced by the difference in mean bond lengths of $d_{\text{StV green}} = (240 \pm 18) \text{ nm}$, compared to $d_{\text{StV blue}} = (213 \pm 18) \text{ nm}$. Regarding coordination number statistics $Z \in \{5, 6, 7, 8\}$, with $Z_{\text{StV green}} = 6.3 \pm 1.0$ and $Z_{\text{StV blue}} = 6.6 \pm 0.9$. None of the listed networks in ref. [38] have valencies ranging from 5 to 8. Therefore, we constructed an initial network by removing some bonds from the body-centered cubic network **bcu** to obtain the modified network **bcu_{mod}** (Figure 3f). Figure 3g compares the coordination number statistics of StV green, StV blue, and **bcu_{mod}**. Similarly, no networks are listed for the network StA orange (Figure 3h) with $Z \in \{3, 4, 5\}$ and $Z_{\text{StA orange}} = 5.0 \pm 0.9$. We remove bonds from the primitive cubic network **pcu**, to obtain the modified network **pcu_{mod}** (Figure 3k). The coordination number statistics of **pcu_{mod}** are comparable to those of the StA orange network (Figure 3l).

We also generated three types of regular disordered networks. The first two types are generated from the cubic diamond **dia** ($Z = 4$, Figure 4a) and the gyroid **srs** ($Z = 3$, Figure 4b). The WWW algorithm has previously been applied to these networks [16, 19, 23, 31]. These networks are of high interest due to their ability to open significant photonic band gaps [60] and their presence in biological structural color materials [34, 61]. The last type starts from the

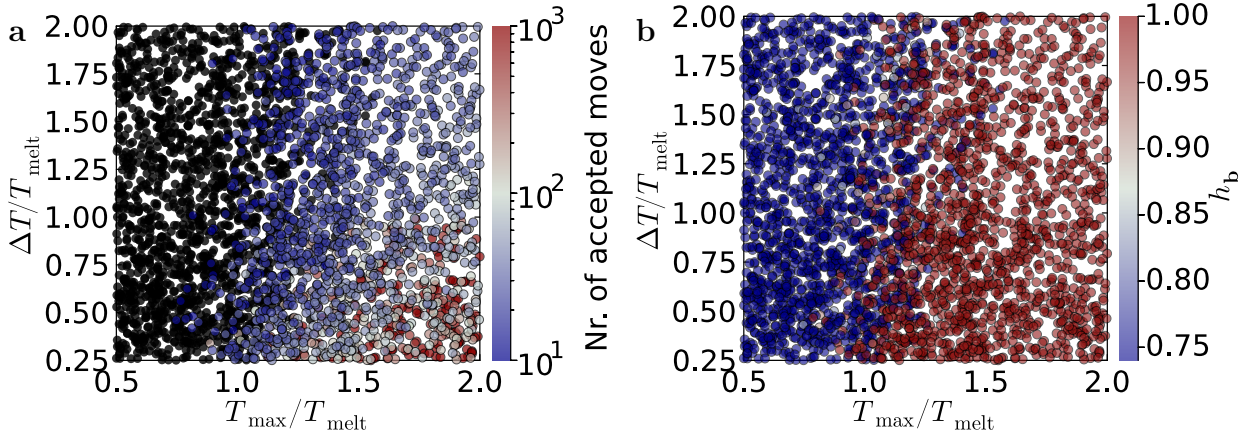


Figure 5: **a** The number of accepted Monte Carlo moves in the **ctn** network increases with increasing maximal heating temperature T_{\max} and with decreasing heating gradient ΔT . The black markers correspond to networks with ten or fewer accepted moves and show that the melting transition begins at $T_{\max} \gtrsim T_{\text{melt}}$. All values of $\beta \in [0, 10]$ are considered. **b** The isotropy metric h_b effectively measures the melting transition of the initial **ctn** network.

4-coordinated **lcs** network (Figure 4c). This network was recently found to have a wide PBG similar to those of **dia** and **srs** [62]. Diamond and the **lcs** networks are interesting to compare because, despite having the same coordination number, their ring statistics and bond angles differ. In summary, we consider six initial networks ranging in valencies from three to eight. In the next section, we investigate how the input parameters of the extended WWW algorithm affect the resulting disordered networks.

4.2 The effect of the parameters on the extended WWW algorithm

Starting from the initial networks presented in Section 4.1, we analyze how the order metrics of the generated networks vary according to the inputs of the extended WWW algorithm. For each initial network, we generate between 450 (for **bcu**_{mod}) and 3,750 (for **ctn**) disordered networks. The input parameter space of the modified WWW algorithm is spanned by β , T_{\max} , and ΔT . We sample random bond-bending constants in the range of $\beta \in [0, 10]$ to vary the ratio of disorder in bond angles and lengths. To sample the melting transition, i.e., the phase transition from crystalline to disordered, we vary the maximum heating temperature and the temperature gradient in units of the β -dependent melting temperature: $T_{\max} \in [T_{\text{melt}}/2, 2T_{\text{melt}}]$, and $\Delta T \in [T_{\text{melt}}/4, 2T_{\text{melt}}]$.

We will now discuss the results for the initial **ctn** network of 224 vertices in detail. Analogous statistics for the other five networks can be found in Appendix B (Figures 19 to 43). The order metrics \bar{q}_l , σ_{q_l} (Section 3.1), A_v (Equation (16)), \bar{s} , and σ_s (Section 3.4) were excluded from the in-depth analysis due to their strong correlation with other metrics. The Steinhardt bond order parameters \bar{q}_l and their standard deviations σ_{q_l} are related to bond-angle disorder σ_θ , but they are more difficult to interpret intuitively. The anisotropy metric A_v is strongly correlated with the analogous metric A_b , which contains more information about the mathematical network. Similarly, the ring sizes \bar{s} and their standard deviations σ_s are closely linked to the ring radii and their standard deviations.

Figure 5a shows the melting transition of the initial **ctn** network. It plots the number of accepted Monte Carlo moves against the heating profile parameters T_{\max} , and ΔT . In this and the following figures, we project the 3D WWW parameter space onto two resolved parameters while considering all values of the third parameter, here β . For low values of T_{\max} , no bond switches are accepted, and the network remains in its initial crystallographic state. The melting

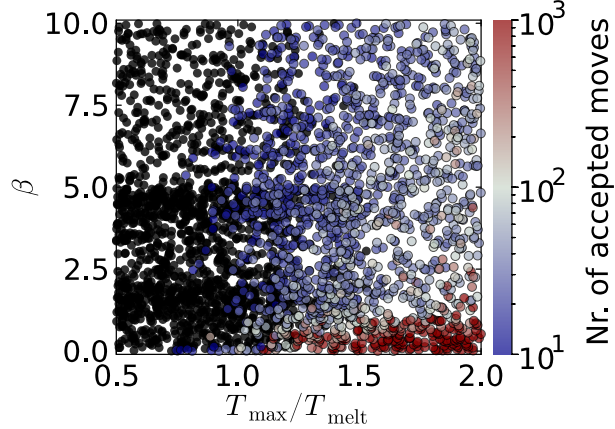


Figure 6: There is an inverse correlation between the bond bending force constant β and the number of accepted Monte Carlo moves when the network is heated above the melting transition $T_{\max} \gtrsim T_{\text{melt}}$. All values of ΔT are considered.

transition occurs close to the melting temperature of Equation (7), $T_{\max} \approx T_{\text{melt}}$. This justifies our somewhat arbitrary definition of T_{melt} given our values of ΔT . We also observe a slight shift of the melting transition to lower values of T_{\max} as ΔT decreases. This behavior corresponds to an increase in accepted moves at low values of ΔT . This reflects the fact that with smaller heating and cooling gradients, more Monte Carlo moves are performed at high temperatures, making melting more probable. The isotropy metrics introduced in Section 3.3, such as bond orientation entropy h_b , are also well-suited to measuring the melting transition as illustrated in Figure 5b. As expected, the crystallographic network with reduced isotropy quickly approaches a statistically isotropic configuration upon melting.

Figure 6 shows the significant effect of the bond bending constant β on the number of accepted Monte Carlo moves when $T_{\max} \gtrsim T_{\text{melt}}$. At small values of $\beta \lesssim 1$, the number of accepted moves exceeds 10^3 , whereas at higher β values, only 10 to 100 moves are accepted. For small β values, the generalized Keating strain energy (Equation (6)) is governed by the bond stretching term E_r , which represents a two-body interaction. The three-body interaction bond bending term E_θ can be neglected. Having a two-body interaction govern the dynamics appears to increase the number of favorable Monte Carlo moves. Even bond chains that are strongly flexed after the bond switch can be accepted if the bond distances relax close to the equilibrium length (Figure 1). In summary, the temperature gradient has a minor influence on the melting behavior, while the maximal temperature and bending constant have a more significant influence on the network statistics. Therefore, we focus on the projection onto these two parameters.

Figure 7 illustrates the impact of the algorithm's input parameters T_{\max} and β on the bond length and angle statistics of the generated networks. Similar to the increase in isotropy with increasing T_{\max} (Figure 5b), the degree of disorder in the bond lengths, as measured by σ_r , generally increases with T_{\max} (Figure 7a). Additionally, there is a strong positive correlation between β and σ_r . As previously mentioned, the low values of σ_r at small β are due to the higher energy penalty for disorder in bond lengths compared to disorder in bond angles. Interestingly, for small values of $\beta \lesssim 0.15$, σ_r approaches 0, similar to the periodic **ctn** network. Counterintuitively, this low degree of disorder is achieved by performing a large number of Monte Carlo moves, as shown in Figure 6. While the initially accepted moves appear to introduce defects into the crystalline system, resulting in higher σ_r values, subsequent moves relax the strain of the defect states, reducing the degree of disorder.

Figure 7b shows a positive correlation between disorder in the bond angles σ_θ and T_{\max} , as well as with β . Unlike σ_r , bond angle standard deviation increases from $\sigma_\theta = 0.106$ in the

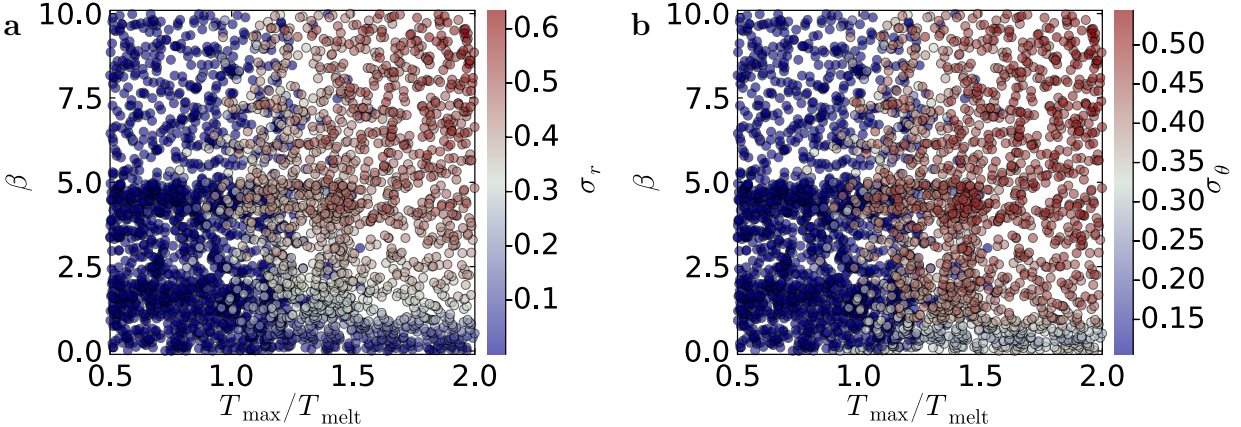


Figure 7: Disorder in the primitives of networks generated from the initial **ctn** network. **a** Disorder in the bond lengths, measured by σ_r , increases with a larger bond bending force constant β and a higher maximal heating temperature T_{\max} . **b** Similarly, disorder in bond angles σ_θ increases with β and T_{\max} . For small β values and large T_{\max} values, σ_r approaches the values of the crystalline network in its melted state. σ_θ is bounded from below by $\sigma_\theta \gtrsim 0.25$. These plots consider all values of ΔT .

crystalline state to $\sigma_\theta \gtrsim 0.25$ at the onset of melting. Lower values are not reached in the disordered state. Since high β values impose a high energy penalty on disorder in bond angles, Figure 6 shows that only a few Monte Carlo moves are accepted at large β values. As discussed above, this is due to three-body interactions in the bond bending energy term E_θ , which reduces the number of favorable bond switches. The small number of accepted Monte Carlo moves makes complete relaxation of the disorder introduced by the first moves unlikely. A more substantial decrease in σ_θ could be achieved through repeated heating and quenching of the network (see Ref. [19]). Starting from a disordered diamond-like network, Barkema et al. achieved disordered networks with $\sigma_\theta \approx 0.175$. However, our disordered networks generated from the crystalline **dia** only achieved values of $\sigma_\theta \approx 0.28$ (see Figure 31b, Appendix B). Unlike **dia** with $\sigma_\theta = 0$, small values of σ_θ are more difficult to achieve from **ctn** due to its mixed coordination number $Z \in \{3, 4\}$.

Figure 7 suggests that well-relaxed, disordered networks are obtained at low values of β and when heated above the melting transition $T_{\max} \gtrsim T_{\text{melt}}$. The two-body bond stretching interaction governing the system allows for a sufficiently high number of accepted Monte Carlo moves to gradually reduce the strain energy. This interpretation is supported by the homogeneity order metrics r_c and r_u plotted in Figures 8a-b. These metrics capture the average distance to the closest vertex and the distance to the closest vertex with which no bond exists, thereby measuring small-scale clustering (Section 3.2). The most ordered networks appear at values of $\beta \lesssim 0.5$.

On the other hand, the critical pore radius δ_c and the hyperuniformity metric α seem to contradict the high-order trend at low β values (Figures 8c-d). A comparison of Figure 8c with Figure 6 shows that the critical pore radius δ_c increases monotonically with the number of accepted Monte Carlo moves. Similarly, only networks around the melting transition are hyperuniform and exhibit $\alpha > 0$, in addition to crystalline and hyperuniform unmelted networks. These observations demonstrate that the Keating strain energy, which governs the Monte Carlo evolution, contains only local and direct space interactions. The critical pore radius measures pore sizes at all length scales, including those that extend beyond the immediate surroundings of individual vertices. Large pores hinder hyperuniformity, which describes large-scale homogeneity [63]. Algorithms in reciprocal space, such as collective coordinate control, are necessary to optimize for hyperuniformity [64]. Nevertheless, our extended WWW algorithm

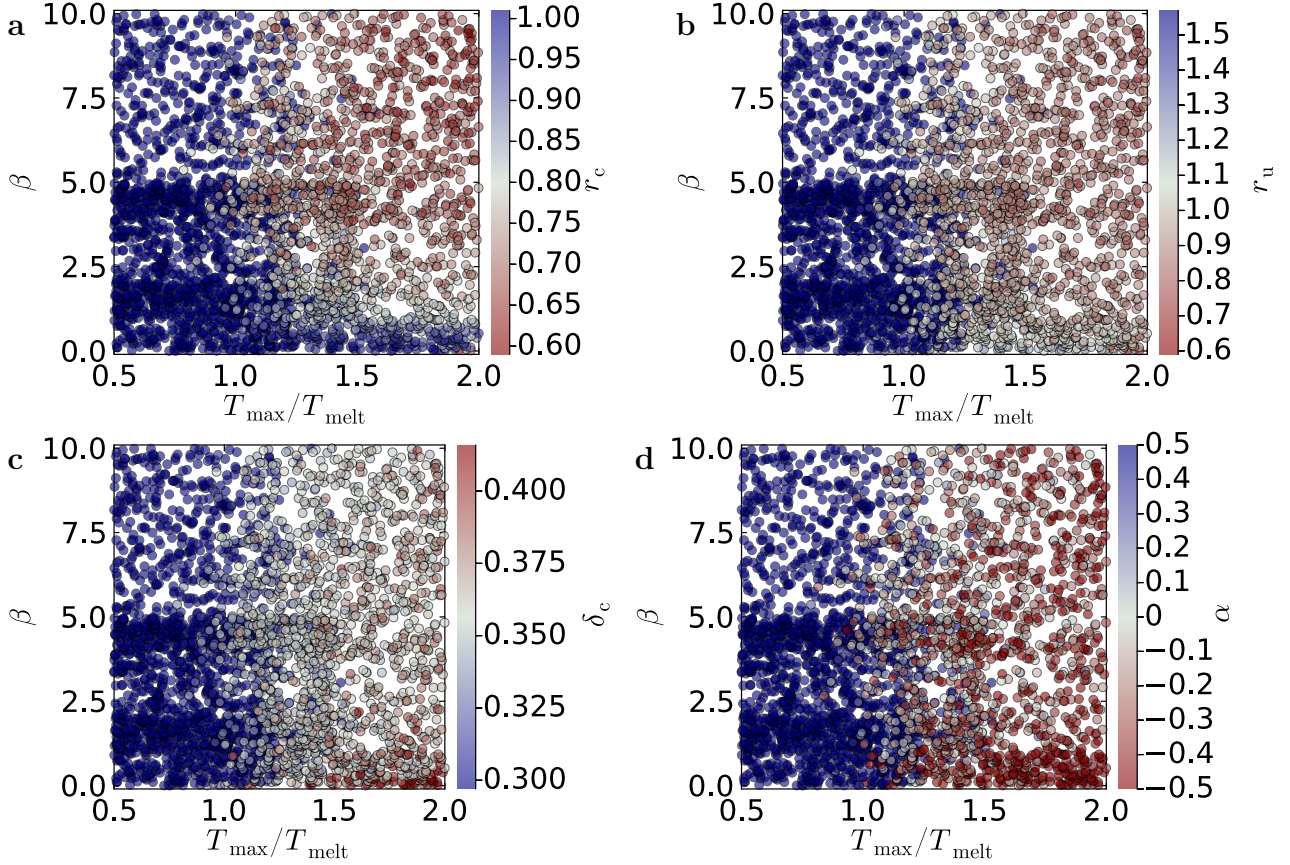


Figure 8: The homogeneity metrics introduced in Section 3.2 are plotted against the algorithm inputs T_{\max} and β for networks generated from the initial **ctn** network. Red colors indicate high disorder with respect to the corresponding metric. **a** The coordinated neighbor distance r_c captures the average distance to the nearest connected neighbor. **b** The uncoordinated neighbor distance r_u measures the average distance to the nearest neighbor that is not coordinated with the reference vertex. **c** The critical pore radius δ_c is the radius of the largest sphere that can percolate a network’s void space. **d** The hyperuniformity metric α is positive for hyperuniform networks.

generates hyperuniform disordered networks, particularly when $1.0 \lesssim T_{\max}/T_{\text{melt}} \lesssim 1.3$.

To conclude, we use the isotropy and topology metrics presented in Sections 3.3 and 3.4, respectively, to analyze how the WWW parameters affect the resulting networks. Figures 9a-b show how the isotropy metrics h_b and A_b fluctuate based on the WWW inputs β and T_{\max} . Both metrics indicate the melting transition, switching from anisotropic to isotropic as soon as the first Monte Carlo moves are accepted. The behavior of the topological metrics \bar{r}_s and σ_{r_s} aligns with that of the local order metrics σ_r , σ_θ , r_c , and r_u . These metrics exhibit maximal order in the disordered state when there are high numbers of bond switches at low values of β . In this regime, the rings vary minimally in radius. The large average ring radii observed in this regime indicate homogeneously distributed vertices and bonds. Small ring radii, on the other hand, are caused by vertex clustering. Based on these observations, we infer that the ring metrics capture small-scale order. Large-scale characteristics are only measured by the critical pore radius and the hyperuniformity metric α .

4.3 Order metric prediction using a neural network

When using the extended WWW algorithm to target a specific set of order metrics, it is helpful to have a computationally efficient method of predicting the outcome based on the inputs. This

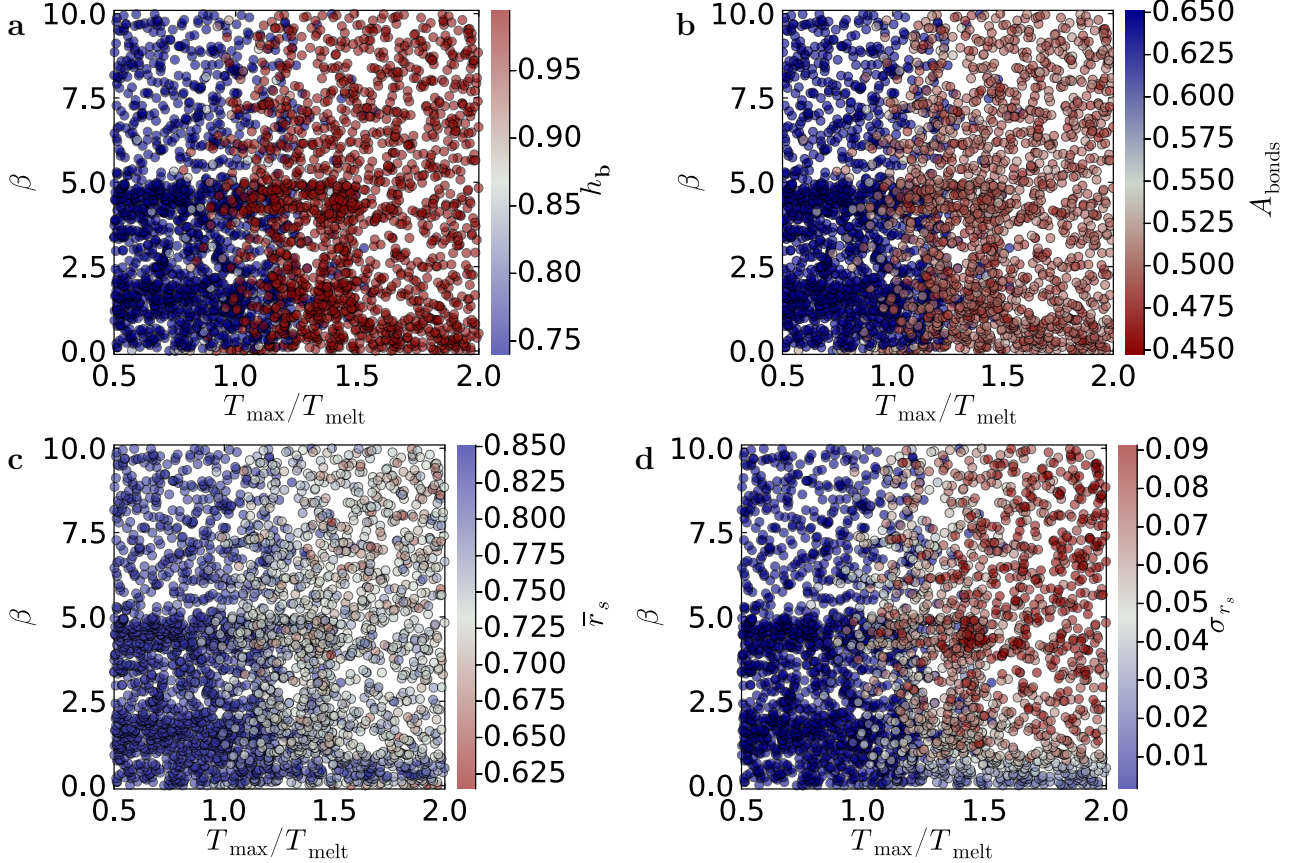


Figure 9: The isotropy and topology metrics of Sections 3.3 3.4 as a functions of the inputs to the network generation algorithm, T_{\max} and β , for networks generated from the initial **ctn** network. Red colors indicate high disorder with respect to the corresponding metric. **a** The isotropy metric bond orientation entropy h_b approaches 1 for isotropic networks. **b** The structure factor anisotropy metric A_b is below 0.6 for isotropic networks. **c** The mean ring radius \bar{r}_s is generally smaller for disordered networks because their vertices tend to cluster, resulting in fewer bonds per ring. **d** The ring radius standard deviation σ_{r_s} quantifies the variation in the diameters of very strong rings. Small values correspond to little disorder in ring sizes.

eliminates the need for trial-and-error network generation, which takes several minutes per network on a single core of an 11th Gen Intel Core i5 processor running at 2.4 GHz. We can write the mapping from algorithm inputs \mathbf{x}_{in} to order metrics $\mathbf{x}_{\text{metric}}$ as

$$f: \mathbb{R}^{N_{\text{in}}} \rightarrow \mathbb{R}^{N_{\text{metric}}}, \quad \mathbf{x}_{\text{in}} \mapsto \mathbf{x}_{\text{metric}},$$

where f is the stochastic function describing the action of the extended WWW algorithm. In our case, after fixing the initial network, $N_{\text{in}} = 3$ (β , T_{\max} , ΔT) and $N_{\text{metric}} = 42$.⁵

We solved the multivariate regression problem of finding an estimator

$$f^*: \mathbf{x}_{\text{in}} \mapsto \mathbf{x}_{\text{metric}}^{\text{predict}}$$

of the true function f by training a fully connected feedforward neural network on a dataset of generated networks. We divided the dataset of 3,750 networks, generated from the initial periodic **ctn**, into three sets: training (70%), validation (15%), and testing (15%). We implemented and trained the network using the PyTorch library [65]. Figure 10 illustrates our network architecture. The input and output dimensionalities determine the number of neurons in the 0th

⁵The list of 42 order metrics is given in Table 2, Appendix A.

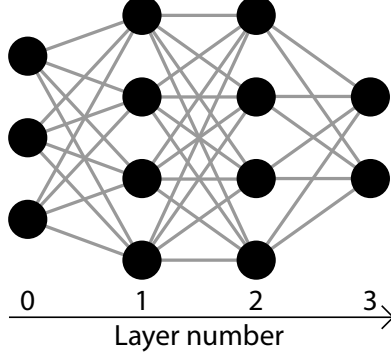


Figure 10: Example of a three-layer ($N_{\text{layers}} = 3$) feedforward neural network. The input layer is counted as 0. The black circles represent neurons and the gray lines depict the data flowing to the right. Our neural network has $N_{\text{in}} = 3$ inputs: β , T_{max} , and ΔT . The number of outputs N_{out} equals the number of order metrics or PCs that the network is trained on. The depicted network has $N_{\text{out}} = 2$ outputs. Between input and output layers, we illustrate two hidden layers, each with $N_{\text{neurons}} = 4$ neurons. N_{layers} , N_{neurons} , and N_{out} are hyperparameters that we optimize.

	Order metric $x_{\text{metric},i}$	Weight w_i
Network primitives	σ_r	0.15
	σ_θ	0.15
	\bar{q}_l for all $l \in \{0, 1, \dots, 12\}$	0.05/13
	σ_{q_l} for all $l \in \{0, 1, \dots, 12\}$	0.05/13
Homogeneity	h_ϕ	0.05
	r_c	0.05
	r_u	0.05
	δ_c	0.10
Isotropy	α	0.02
	h_b	0.10
	A_v	0.05
	A_b	0.05
Topology	\bar{Z}	0.01
	σ_Z	0.01
	\bar{s}	0.005
	σ_s	0.005
	\bar{r}_s	0.05
	σ_{r_s}	0.05

Table 1: We use a weighted mean-squared error loss function with given weights for all order metrics to evaluate the neural network’s prediction accuracy. These weights are selected to balance the varying ranges of the order metrics and treat different order metric groups equally (see Section 3).

input layer and the final output layer, which has an index of N_{layers} ⁶. Between these two layers, we placed $N_{\text{layers}} - 1$ layers, each with N_{neurons} neurons. Each neuron in layers 0 to $N_{\text{layers}} - 1$ has a rectified linear unit (ReLU) activation function.

We use a weighted mean-squared error loss function to evaluate the performance of our neural network and adjust its hyperparameters. The loss function weights w_i are selected to

⁶Following the convention of counting layers after the input layer, we indexed the input layer as zero and the final layer as N_{layers} .

balance the order metric groups and to compensate for their varying value ranges (Table 1). Network accuracy is measured by the average loss on the test dataset. The best-performing network is achieved through preprocessing of the order metric data. First, we scale each order metric data component of $\mathbf{x}_{\text{metric}}$ to a mean value of 0 and a standard deviation of 1. Then, we reduce its dimensionality using principal component analysis (PCA) [66–68]. The optimal number of principal components (PCs) N_{PC} depends on the level of correlation and noise in the data. The more correlated the dimensions of the data are, the fewer PCs are needed to incorporate a sufficient amount of information. Furthermore, in noisy data, PCs above a certain threshold represent more noise than useful information. Therefore, dimensionality reduction prevents overfitting. There are several methods to estimate the optimal number of PCs. One method is to set a cumulative percentage threshold of total variation, and another is to use cross-validation [66]. We use an unweighted mean-squared error loss function to train on preprocessed order metric data. Then, we select the number of PCs that yields the best performance on the test data, as measured by a weighted mean-squared error loss function.

We perform hyperparameter tuning through random sampling. The hyperparameters N_{layers} and N_{neurons} determine the network’s architecture. Other hyperparameters include the learning rate η and the batch size N_{batch} , which influence the training process ⁷. Furthermore, we train on data with and without preprocessing (see above). For preprocessed data, we vary the number of PCs N_{PC} . The lowest test loss is achieved with

$$\eta = 0.005 \quad , \quad N_{\text{batch}} = 1 \quad , \quad N_{\text{layers}} = 4 \quad , \quad N_{\text{neurons}} = 72 \quad \text{and} \quad N_{\text{PC}} = 10 \quad .$$

Figure 11 shows the cumulative explained variance as a function of the number of PCs, along with the absolute values of their order metric loadings. The first PC explains 83% of the total variance in the order metrics (Figure 11a) and has nearly equal loadings for all metrics (Figure 11b), indicating strong correlations. The only deviations are the loadings of the Steinhardt parameters and their standard deviations. For clarity, we combine them into single values, denoted by $\bar{\mathbf{q}}$ and $\sigma_{\mathbf{q}}$. These are the norms of the loading vectors in the two subspaces spanned by the q_l and σ_{q_l} , $l \in \{0, 1, \dots, 12\}$. We find that σ_{q_4} , σ_{q_7} , $\sigma_{q_{10}}$, and $\sigma_{q_{11}}$ predominantly contribute to the high loadings of $\sigma_{\mathbf{q}}$ (Figure 44, Appendix B). For the **ctn** network, these metrics indicate the transition from the crystalline to the disordered phase. Higher-order PCs can be assigned to groups of metrics representing different network features. The second PC contains information about small-length-scale features, and the third PC explains intermediate-scale characteristics. The fourth PC contains metrics related to Steinhardt’s local bond order parameters (Figure 44, Appendix C), while higher PCs focus on rings and isotropy.

Figures 12, 13, and 14 show the order metric predictions of the tuned and trained neural network. Comparing these figures with the true order metrics in Figures 7, 8, and 9 shows that the order and disorder regimes are accurately reproduced for all metrics. In all figures, the melting transition at $T_{\text{max}} \approx T_{\text{melt}}$ is clearly visible. As with the true data, the metrics can be divided according to their behavior in the $T_{\text{max}} \gtrsim T_{\text{melt}}$ and $\beta \lesssim 0.5$ input parameter regime. Order metrics that measure small length scales indicate high order, while large-scale homogeneity metrics δ_c and α indicate high disorder. An interesting intermediate regime exists for $\beta \lesssim 1.5$ and $T_{\text{max}} \approx 1.5T_{\text{melt}}$. In this regime, networks are expected to become disordered and isotropic yet remain hyperuniform.

The coefficient of determination is a measure of a neural network’s prediction accuracy. Since the output of the extended WWW algorithm exhibits strong statistical fluctuations that hinder accurate predictions, the coefficient quantifies the variance in the order metrics $\mathbf{x}_{\text{metric}}$ for the

⁷For more information about neural network training parameters, please refer to the PyTorch documentation [69].

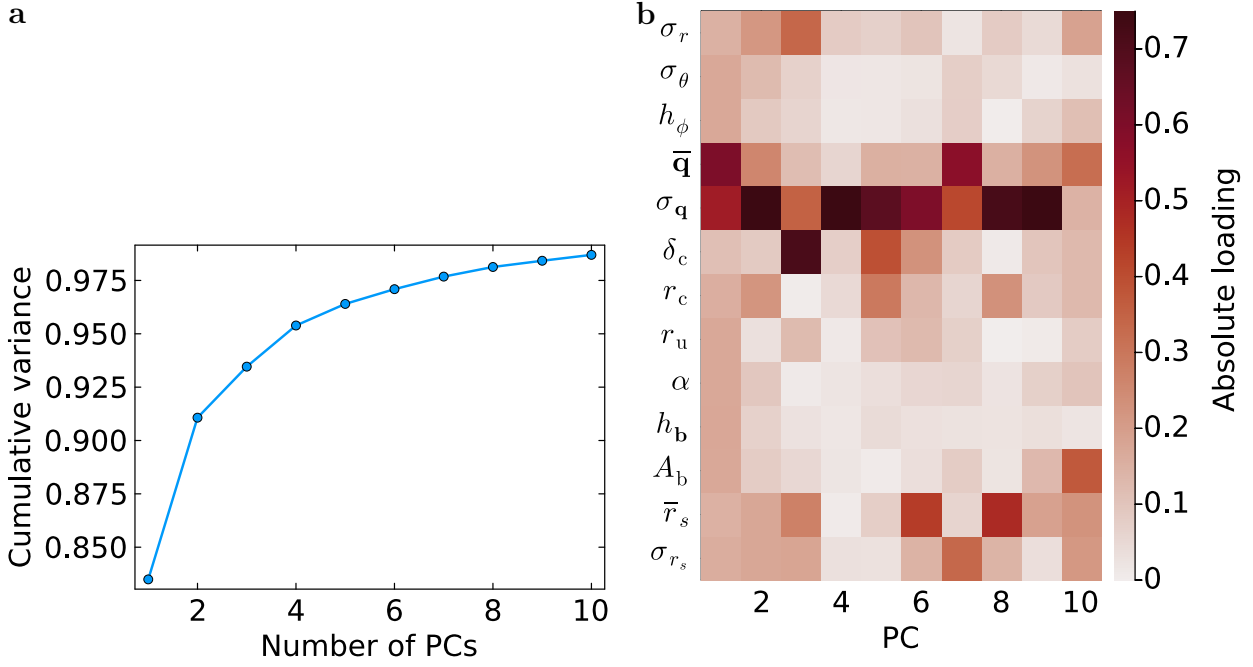


Figure 11: Training the neural network using ten PCs representing 42 order metrics yields higher prediction accuracy than using the full dataset. **a** The first PC explains 83% of the variance in the order metrics. The first ten PCs explain 99% of the variance and produce the best network performance, suggesting that the remaining 1% consist primarily of noise. **b** Absolute values of the PCA loadings when considering all order metrics. For the Steinhardt parameters, we depict the norm of the vectors $\bar{\mathbf{q}}$ and $\sigma_{\mathbf{q}}$, whose components are the loadings of \bar{q}_l and σ_{q_l} , $l \in \{0, 1, \dots, 12\}$. Combining 13 metrics into one norm results in their prominent magnitudes in the heatmap. Besides $\bar{\mathbf{q}}$ and $\sigma_{\mathbf{q}}$, the first PC is loaded with approximately equal contributions from all order metrics. Higher PCs reveal correlations between the order metrics. For example, the second PC shows correlations between the small-length-scale metrics. Since Z and σ_z remain constant throughout the dataset, their vanishing PC loadings are not shown.

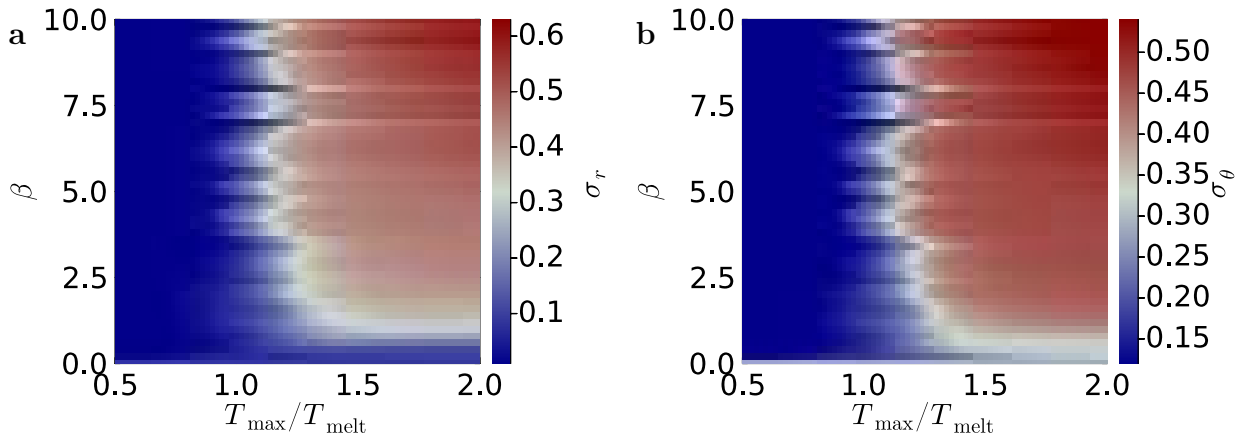


Figure 12: Neural network predictions of the order metrics describing primitives for networks generated from the initial **ctn** network. The noise in the transition from crystalline state to melted networks originates from energy fluctuations in the definition of the melting temperature (Equation (7)). An intermediate temperature gradient $\Delta T = T_{\max}/2$ was set because it has a negligible effect on the order metrics (see Section 4.2). **a** The bond length standard deviation prediction can be compared to the actual data in Figure 7a. **b** The bond angle standard deviation prediction can be compared to the actual data in Figure 7b.

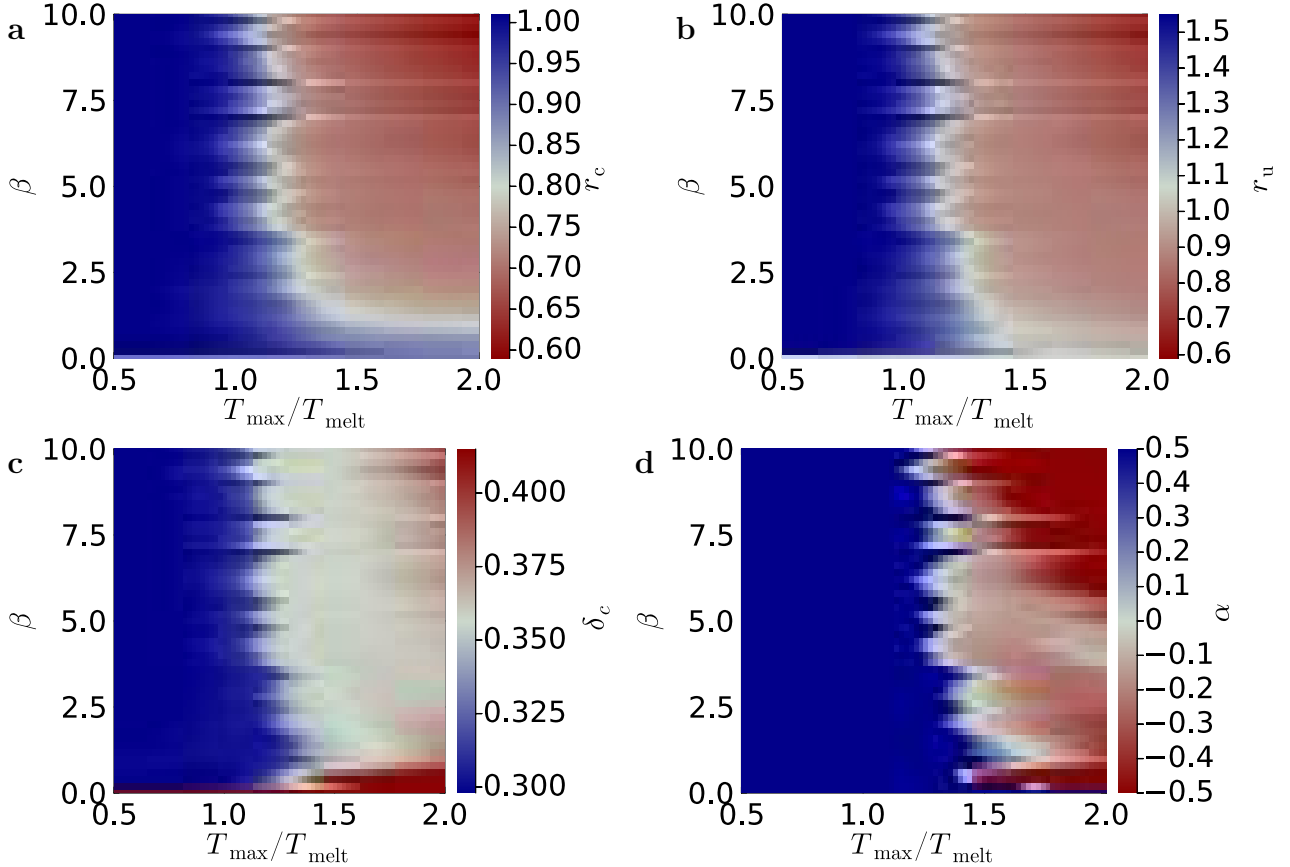


Figure 13: Neural network predictions of the order metrics describing homogeneity for networks generated from the initial **ctn** network. The noise in the transition from crystalline state to melted state originates from energy fluctuations in the definition of the melting temperature (Equation (7)). An intermediate temperature gradient $\Delta T = T_{\max}/2$ was set because it has a negligible effect on the order metrics (see Section 4.2). **a** The vertex homogeneity prediction can be compared to the actual data in Figure 8a. **b** The uncoordinated neighbor distance prediction can be compared to the actual data in Figure 8b. **c** The critical pore radius prediction can be compared to the actual data in Figure 8c. **d** The hyperuniformity metric α prediction can be compared to the actual data in Figure 8d.

same input values \mathbf{x}_{in} . The coefficient of determination [70]

$$R^2 = 1 - \frac{\sum_i (x_{\text{metric},i} - x_{\text{metric},i}^{\text{predict}})^2}{\sum_i (x_{\text{metric},i} - \bar{x}_{\text{metric}})^2}$$

represents the proportion of the variance in the data explained by the prediction. In our case, it is calculated for each order metric individually. The index i runs over all networks generated in the test set. $x_{\text{metric},i}^{\text{predict}}$ is the predicted order metric for network i . The corresponding true metric is $x_{\text{metric},i}$, and \bar{x}_{metric} is the mean order metric value in the test dataset. $R^2 = 1$ for perfect predictions and $R^2 \leq 0$ for random predictions.

Figure 15 plots R^2 for all considered order metrics. Since the coordination number is constant for all networks, $R^2 = 1$ for the corresponding metrics \bar{Z} and σ_Z . In addition to the coordination number metrics, the neural network achieves maximum determination with the small-scale order metrics σ_r , σ_θ , and σ_{r_s} . The high values for $R^2(\sigma_r) = 0.82$ and $R^2(\sigma_\theta) = 0.79$ are explained by the fact that bond lengths and angles are directly controlled by the generalized Keating energy (Equation (6)), which governs the network evolution. However, the high degree of control over disorder in ring radii, quantified by $R^2(\sigma_{r_s}) = 0.83$, is less evident, especially since mean ring radii exhibit low determination with $R^2(\bar{r}_s) = 0.62$. This suggests little correlation between

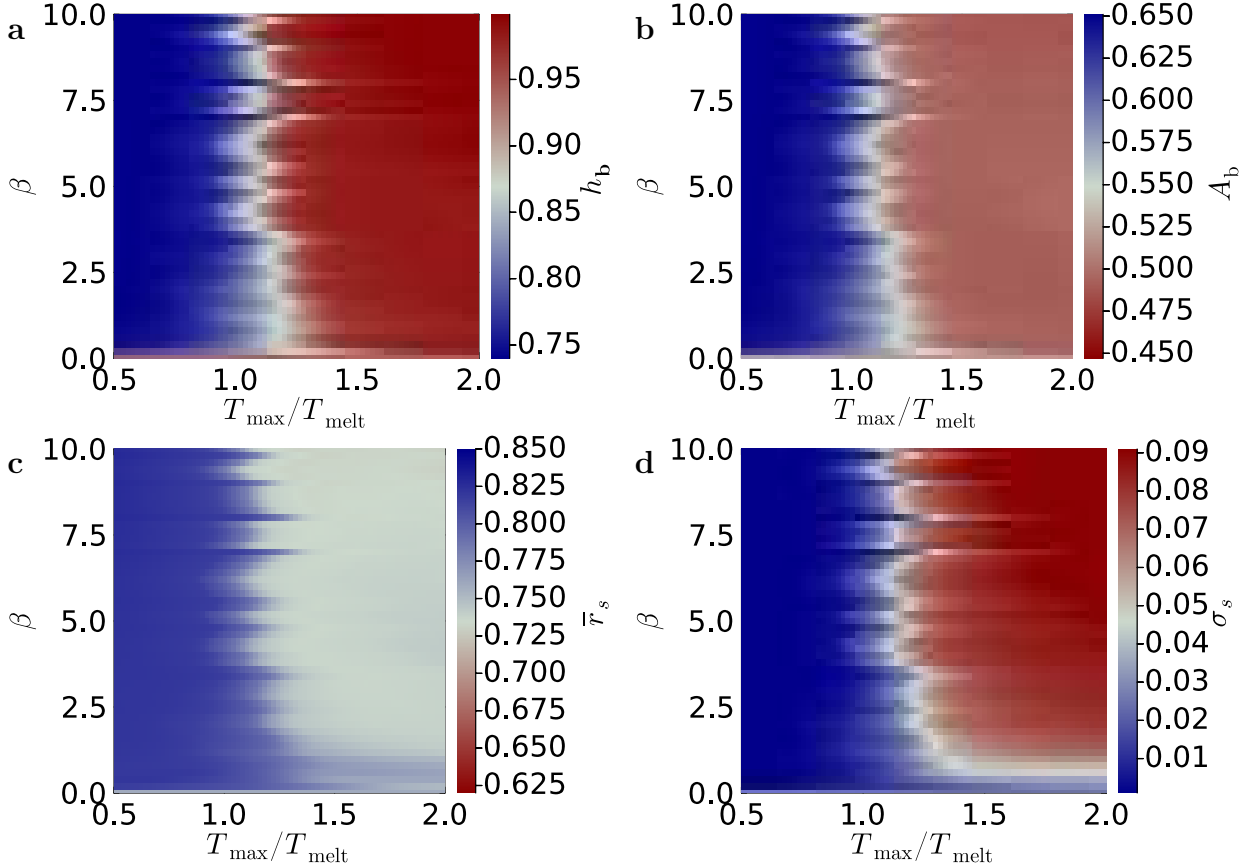


Figure 14: Neural network predictions of the order metrics describing isotropy and topology for networks generated from the initial **ctn** network. The noise in the transition from crystalline state to melted state originates from energy fluctuations in the definition of the melting temperature Equation (7)). An intermediate temperature gradient $\Delta T = T_{\max}/2$ was set because it has a negligible effect on the order metrics (see Section 4.2). **a** The bond orientation entropy prediction can be compared to the actual data in Figure 9a. **b** The structure factor anisotropy metric prediction can be compared to the actual data in Figure 9b. **c** The mean ring radius prediction can be compared to the actual data in Figure 9c. **d** The ring radius standard deviation prediction can be compared to the actual data in Figure 9d.

\bar{r}_s and σ_{r_s} . This is supported by the relatively independent PC loadings of the two variables (Figure 11b).

Besides the mean ring radius, the critical pore radius has the lowest coefficient of determination $R^2(\delta_c) = 0.6$. This metric captures homogeneity at all length scales and is sensitive to pore opening. Since the Keating energy does not control this process, there is significant variance in δ_c despite identical input parameters. This leads to inaccurate neural network predictions. However, we have now developed the necessary tools to reproduce the biological networks introduced in Section 4.1.

4.4 Reproducing disordered biophotonic networks

In this section, we identify generated networks that resemble the biological geometries introduced in Section 4.1 by comparing their respective order metrics, as discussed in Section 3. Section 4.3 assessed the neural network’s order metric prediction accuracy using a weighted mean square error loss function with weights w_i , provided in Table 1. We define an *order distance metric*

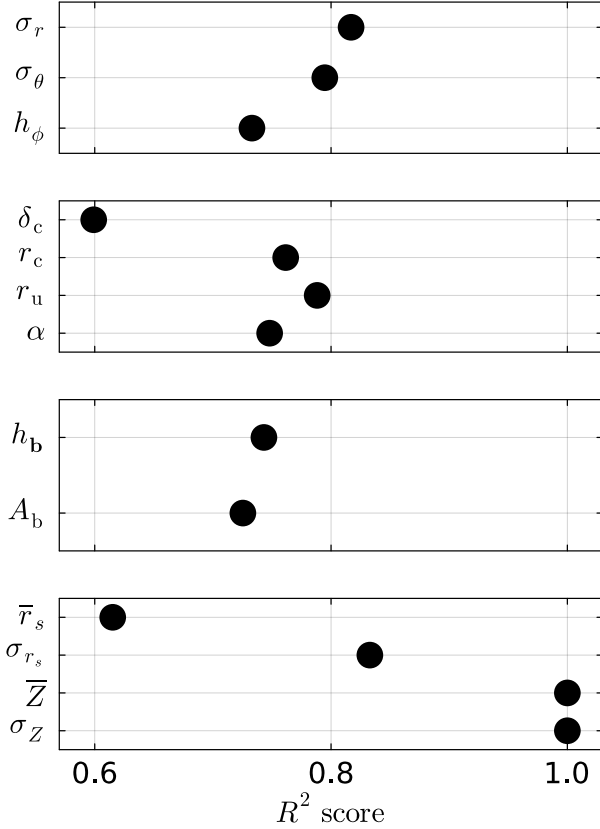


Figure 15: The coefficient of determination R^2 measures the accuracy of a neural network’s predictions. It indirectly quantifies the variance in the order metrics of the generated networks when using the same generation algorithm inputs.

between two networks with the same functional form to quantify their structural similarity,

$$d_{\text{order}} = \left[\sum_{i=1}^{N_{\text{metric}}} w_i (x_{\text{metric},i}^{\text{net 2}} - x_{\text{metric},i}^{\text{net 1}})^2 \right]^{\frac{1}{2}}. \quad (17)$$

We now identify the generated networks with the smallest order distance metric compared to biological networks. Figure 16a shows the network **ctn_{PCM blue}**, which is the generated network closest to PCM blue. It is obtained by evolving the **ctn** network with 224 vertices with WWW parameters

$$\beta = 6.3359, \quad T_{\max} = 8.607 = 1.334 T_{\text{melt}} \quad \text{and} \quad \Delta T = 11.717 = 1.543 T_{\text{melt}}.$$

The original **ctn** network was modified with 87 accepted Monte Carlo moves. Since each bond switch involves a chain of four vertices, each vertex was included in approximately 1.5 bond switches.

Figure 16b shows the high level of agreement between the biological and the generated network. This is evident through the order metric comparison between **ctn_{PCM blue}** and PCM blue. A comparison of Figure 16b with Figures 7 and 8 shows that **ctn_{PCM blue}** is an intermediate disorder network with respect to σ_r and σ_θ , which describe network primitives. However, with respect to the homogeneity metrics δ_c , r_u , and especially α , the order metric values of PCM blue approach the limits of what can be achieved with the extended WWW algorithm. This is because the Keating strain energy does not penalize disorder in these homogeneity metrics. Nevertheless, **ctn_{PCM blue}** achieves homogeneity values similar to those of PCM blue.

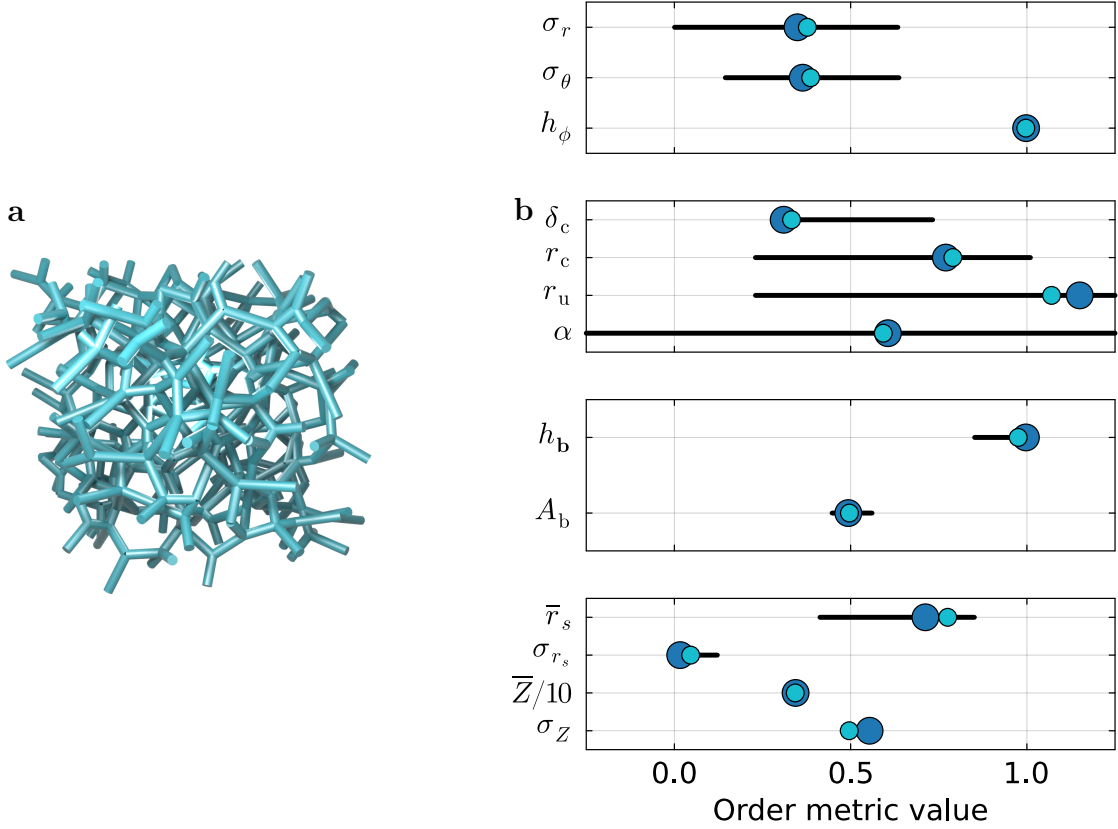


Figure 16: **a** The network with the shortest order metric distance to the PCM blue biophotonic network (Figure 3a) was generated from an initial **ctn** network. **b** The order metric values of the network generated in **a** (small light blue markers) closely match those of the PCM blue biophotonic network (large dark blue markers). The black bars represent the order metrics ranges achieved by modifying the initial **ctn** network with at least ten accepted Monte Carlo moves.

Furthermore, we reproduce the biophotonic structures of the beetle *Sternotomini virescens* (StV green and Stv blue in Figure 3l-b). The StV green structure is best reproduced by the **bcu_{StV green}** network (Figure 17a), generated from the periodic **bcu_{mod}** network with 432 vertices, with WWW parameters

$$\beta = 0.0018 \quad , \quad T_{\max} = 0.2401 = 0.591 T_{\text{melt}} \quad \text{and} \quad \Delta T = 0.3271 = 0.805 T_{\text{melt}} \quad .$$

These parameters resulted in 340 accepted Monte Carlo moves, with every vertex involved in approximately 3.1 accepted moves. Similarly, network **bcu_{StV blue}** (Figure 17b) – the network closest to Stv blue – was generated with

$$\beta = 0.0012 \quad , \quad T_{\max} = 0.2314 = 0.678 T_{\text{melt}} \quad \text{and} \quad \Delta T = 0.4296 = 1.260 T_{\text{melt}} \quad .$$

This resulted in 329 accepted Monte Carlo moves, three per vertex.

Figure 17c shows good agreement between the order metrics of the generated networks **bcu_{StV green}** and **bcu_{StV blue}**, and the corresponding biological networks. The most significant discrepancy is in the coordination number standard deviation σ_Z , which is determined by the initial network. Figure 3k shows that our choice of the initial network **bcu_{mod}** has a simplified coordination number histogram that neglects the high- and low-coordination number tails of the biological networks.

Besides σ_Z , the homogeneity metrics r_u and α differ significantly between generated and biological samples. The coordinated neighbor distance r_c is strongly influenced by the bond

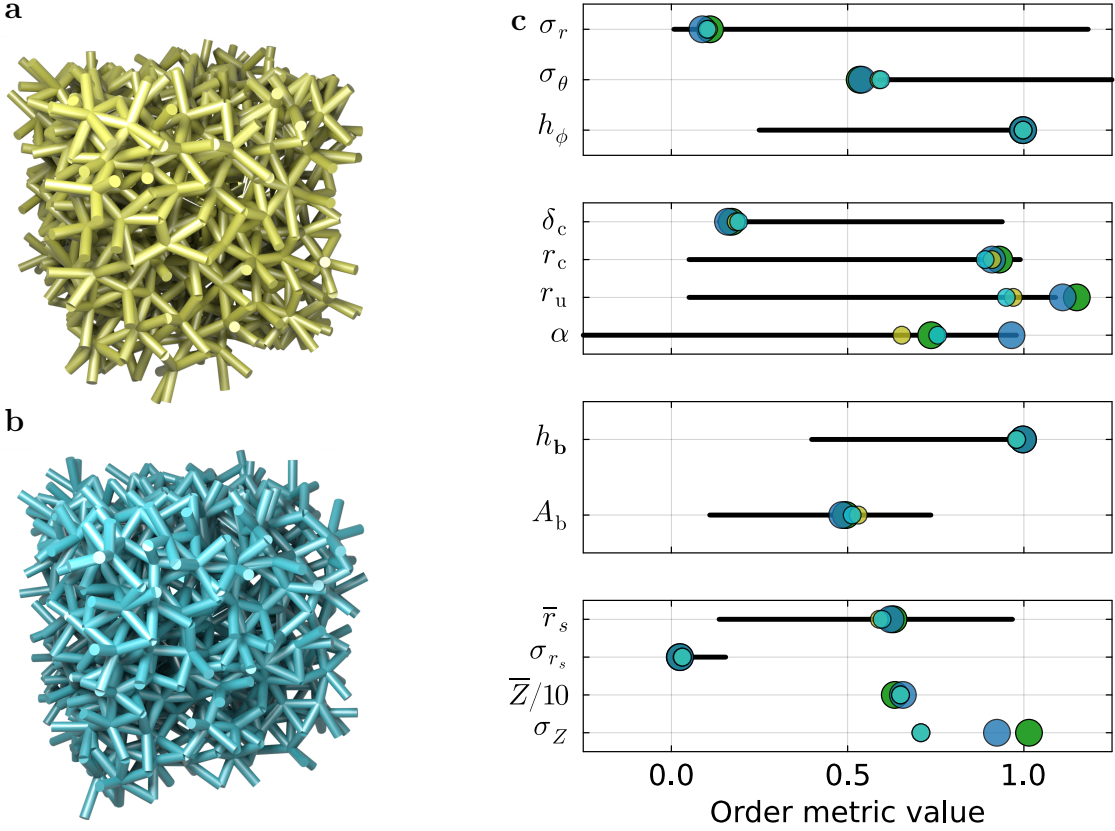


Figure 17: **a** The generated network $\mathbf{bcu}_{\text{StV green}}$ has the smallest order metric distance to the StV green biological network (Figure 3l). It was generated from an initial $\mathbf{bcu}_{\text{mod}}$ network. **b** The generated network $\mathbf{bcu}_{\text{StV blue}}$ is the most similar to StV green (Figure 3e). **c** The order metric values of networks $\mathbf{bcu}_{\text{StV green}}$ (**a**, small olive green markers) and $\mathbf{bcu}_{\text{StV blue}}$ (**b**, small light blue markers) closely match the biophotonic network metrics of StV green (large green markers) and StV blue (large dark blue markers). The black bars represent the ranges of order metrics achieved by modifying the initial $\mathbf{bcu}_{\text{mod}}$ network with at least ten accepted Monte Carlo moves.

stretching term E_r in Equation (2). However, the bond stretching term has no effect on r_u , the average distance to the closest vertex with which no bond exists. Therefore, the network’s Monte Carlo evolution can produce local clusters of unconnected vertices, reducing r_u . Figures 8b and 13b show that networks generated with small β values have the greatest disorder and homogeneity with respect to r_u . Examples of these networks are $\mathbf{bcu}_{\text{StV green}}$ and $\mathbf{bcu}_{\text{StV blue}}$. As discussed in Section 4.2, similarly to r_u , the hyperuniformity metric is not directly affected by the Keating energy. Therefore, α generally decreases with every accepted Monte Carlo move.

The third biological network StA orange, introduced in Section 4.1, was reproduced from the initial $\mathbf{pcu}_{\text{mod}}$ network with the algorithm inputs

$$\beta = 0.0978 \quad , \quad T_{\max} = 0.1788 = 1.034 T_{\text{melt}} \quad \text{and} \quad \Delta T = 0.1858 = 1.074 T_{\text{melt}} \quad .$$

These inputs resulted in 689 accepted Monte Carlo moves, meaning each vertex was involved in an average of 13 bond switches. Figure 18a shows the resulting disordered network, and Figure 18b compares its order metric values to those of the biological network. Similar trends to those observed in the reproduction of the StV networks in Figure 17c are seen here. While the small-scale and isotropy order metrics are well reproduced, the intermediate and large-scale homogeneity metrics differ significantly between biological and generated networks. As previously discussed, this discrepancy is due to the Keating energy, which is limited to short

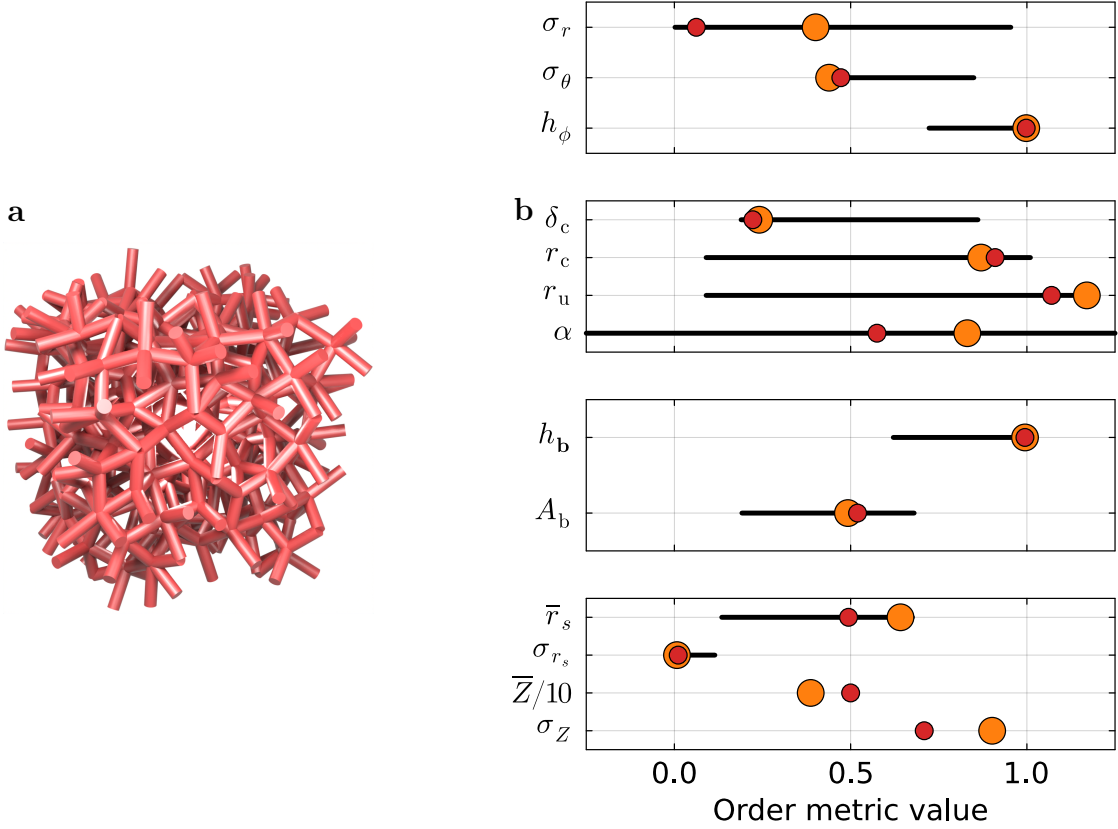


Figure 18: **a** The network with the smallest order metric distance to the Sta orange biological network (Figure 3e) was generated from an initial $\mathbf{pcu}_{\text{mod}}$ network. **b** The order metric values of the network in **a** (small red markers) closely match those of the Sta orange biophotonic network (large orange markers). The black bars represent the range of order metrics achieved by modifying the initial $\mathbf{pcu}_{\text{mod}}$ network with at least ten accepted Monte Carlo moves.

length scales in its current form.

Despite minor deviations in the homogeneity metrics, we conclude that our extended WWW algorithm successfully reproduces all disordered biophotonic networks. We achieved this by matching the coordination number statistics of the target networks with those of an initially crystalline network. Additionally, we created network datasets by randomly sampling the algorithm’s input parameters. The resulting disordered networks span a wide range of order metric values, as apparent from all figures in Sections 4.2 and 4.4. Although the generalized Keating energy provides significant control over short-length-scale metrics, higher variance is observed in longer-ranged metrics related to pore sizes and hyperuniformity.

5 Conclusion

Computer-generated disordered spatial networks are essential to many fields in the natural and social sciences. We modified the Keating strain energy to adapt the existing WWW algorithm to networks with arbitrary coordination number statistics. We also adjusted the degree of disorder in the generated networks by modifying the bond-bending force constant and the temperature profile governing the Monte Carlo evolution in the Keating energy. To analyze the effect of these adjustments on the resulting networks, we introduced an extensive set of order metrics covering network primitives, homogeneity, isotopy, and topology.

As a case study, we statistically reproduced four disordered biophotonic networks responsible for structural color in various beetles. Starting with six crystalline networks, we randomly sampled the algorithm inputs to generate datasets containing thousands of disordered networks. Next, we trained a feedforward neural network to predict order metrics derived from the algorithm’s inputs. Our results show that the Keating energy enables precise control over short-range order metrics by quantifying disorder in bond lengths and angles. However, we observed higher statistical variance in long-range metrics that measure pore sizes and hyperuniformity.

This work paves the way for studying the relationship between the structure of disordered spatial networks and their properties. Optical simulations on the generated network datasets are an essential next step in understanding structural color in disordered photonic materials. Observing the effects of individual order metrics on the reflectance spectra obtained with finite-difference time-domain simulations will reveal the relevant correlations between structural and optical properties.

Further understanding can be gained from the photonic densities of states (PDOS). The PDOS can either be obtained through voxelization of the photonic network and a plane-wave method [71], or by decorating the material with dipoles and using a Green’s matrix method [72]. We expect insights from the emergence of photonic band gaps (PBGs), defect states within the PBG, and localized edge modes [73]. Considering emission in disordered networks could lead to the onset of random lasing, deepening the understanding of how to generate and control complex lasing spectra [74]. Furthermore, training a neural network on the resulting datasets will enable the prediction of optical properties from structural information, providing a highly efficient alternative to optical simulations.

Beyond photonic materials, the extended WWW algorithm and the order metrics presented in this work can be applied to disordered spatial networks in any field of research. The generated datasets can be tailored to the desired application by selecting an appropriate initial network and adjusting the temperature profile. Additional terms can be added to the generalized strain energy to emphasize the desired order metrics. Including reciprocal space metrics into the strain energy would yield direct control over wave scattering phenomena, albeit at the cost of increased computational complexity.

Acknowledgments

The authors thank Niklas R. Schwarz for the data preprocessing of the *Sternotomis amabilis* beetle photonic network. The authors thank Viola V. Vogler-Neuling for helpful discussions about biophotonic materials and Luis S. Froufe-Pérez for valuable input about neural networks. This study was supported by a European Research Council (ERC) Advanced grant (PrISMoID, 833895), the Adolphe Merkle Foundation, and the Swiss National Science Foundation (SNSF) through the National Center of Competence in Research Bio-Inspired Materials (grant no. 51NF40-182881).

Data Availability Statement The data that support the findings of this study are openly available on Zenodo [75]. The source code supporting this work is available on GitHub [76].

References

- [1] J. Medvedeva, D. Buchholz, R. Chang, *Advanced Electronic Materials* **2017**, *3* 1700082.
- [2] Y. Gu, J. Zhao, J. A. Johnson, *Angewandte Chemie International Edition* **2020**, *59*, 13 5022.
- [3] K. Vynck, R. Pierrat, R. Carminati, L. S. Froufe-Pérez, F. Scheffold, R. Sapienza, S. Vignolini, J. J. Sáenz, *Reviews of Modern Physics* **2023**, *95*, 4 045003, publisher: American Physical Society.
- [4] C. W. Lynn, D. S. Bassett, *Nature Reviews Physics* **2019**, *1*, 5 318.
- [5] J. Wang, X. Huang, J. Xu, Z. Zhang, S. Wang, Y. Li, *Engineering Geology* **2023**, *318* 107103.
- [6] T. Anderson, S. Dragićević, *Geography Compass* **2020**, *14*, 9 e12502.
- [7] H. Akbari, *Social Networks* **2021**, *64* 181.
- [8] C. Gan, M. Voda, K. Wang, L. Chen, J. Ye, *Journal of Hospitality and Tourism Management* **2021**, *47* 124.
- [9] J. Jackle, *Reports on Progress in Physics* **1986**, *49*, 2 171.
- [10] L. Berthier, D. R. Reichman, *Nature Reviews Physics* **2023**, *5*, 2 102, publisher: Nature Publishing Group.
- [11] S. Zhang, F. Zhao, J. Chen, J. Fu, J. Luo, S. H. Alahakoon, L.-Y. Chang, R. Feng, M. Shakouri, J. Liang, Y. Zhao, X. Li, L. He, Y. Huang, T. K. Sham, X. A. Sun, *Nature Communications* **2023**, *14*.
- [12] Y. Zhu, Z. D. Hood, H. Paik, P. B. Groszewicz, S. P. Emge, F. N. Sayed, C. Sun, M. Balaish, D. Ehre, L. J. Miara, A. I. Frenkel, I. Lubomirsky, C. P. Grey, J. L. M. Rupp, *Matter* **2024**, *7*, 2 500.
- [13] K. Edagawa, S. Kanoko, M. Notomi, *Physical Review Letters* **2008**, *100*, 1 013901.
- [14] F. Scheffold, J. Haberko, S. Magkiriadou, L. S. Froufe-Pérez, *Physical Review Letters* **2022**, *129*, 15 157402.
- [15] M. E. J. Newman, G. T. Barkema, *Monte Carlo Methods in Statistical Physics*, Oxford University Press, **1999**.

- [16] F. Wooten, K. Winer, D. Weaire, *Physical Review Letters* **1985**, *54*, 13 1392, publisher: American Physical Society.
- [17] W. H. Zachariasen, *Journal of the American Chemical Society* **1932**, *54*, 10 3841, publisher: American Chemical Society.
- [18] L. P. O'Mard, *Modelling and Simulation in Materials Science and Engineering* **1993**, *1*, 4 485.
- [19] G. T. Barkema, N. Mousseau, *Physical Review B* **2000**, *62*, 8 4985.
- [20] Y. Tu, J. Tersoff, G. Grinstein, D. Vanderbilt, *Physical Review Letters* **1998**, *81*, 22 4899, publisher: American Physical Society.
- [21] S. M. Nakhmanson, N. Mousseau, *Journal of Physics: Condensed Matter* **2002**, *14*, 26 6627.
- [22] R. L. C. Vink, *The Journal of Chemical Physics* **2014**, *140*, 10 104509.
- [23] B. R. Djordjević, M. F. Thorpe, F. Wooten, *Physical Review B* **1995**, *52*, 8 5685, publisher: American Physical Society.
- [24] R. L. C. Vink, G. T. Barkema, M. A. Stijnman, R. H. Bisseling, *Phys. Rev. B* **2001**, *64* 245214.
- [25] R. L. C. Vink, G. T. Barkema, *Physical Review B* **2003**, *67*, 24 245201, publisher: American Physical Society.
- [26] Y. Tu, J. Tersoff, *Physical Review Letters* **2000**, *84*, 19 4393, publisher: American Physical Society.
- [27] R. Cabriolu, M. G. D. Pópolo, P. Ballone, *Physical Chemistry Chemical Physics* **2009**, *11*, 46 10820, publisher: The Royal Society of Chemistry.
- [28] P. N. Keating, *Physical Review* **1966**, *145*, 2 637, publisher: American Physical Society.
- [29] F. H. Stillinger, T. A. Weber, *Phys. Rev. B* **1985**, *31* 5262.
- [30] M. H. J. Bailey, D. O. Morley, M. Wilson, *RSC Advances* **2020**, *10*, 63 38275, publisher: The Royal Society of Chemistry.
- [31] S. R. Sellers, W. Man, S. Sahba, M. Florescu, *Nature Communications* **2017**, *8*, 1 14439.
- [32] O. Delgado-Friedrichs, M. O'Keeffe, srd, **2025**, URL <http://rcsr.net/nets/ctn>.
- [33] H. Yin, B. Dong, X. Liu, T. Zhan, L. Shi, J. Zi, E. Yablonovitch, *Proceedings of the National Academy of Sciences* **2012**, *109*, 27 10798.
- [34] K. Djeghdi, U. Steiner, B. D. Wilts, *Advanced Science* **2022**, *9*, 26 2202145, eprint: <https://onlinelibrary.wiley.com/doi/pdf/10.1002/advs.202202145>.
- [35] V. V. Vogler-Neuling, M. Saba, I. Gunkel, J. O. Zoppe, U. Steiner, B. D. Wilts, A. Dodero, *Advanced Functional Materials* **2023**, 2306528.
- [36] V. Bauernfeind, K. Djeghdi, I. Gunkel, U. Steiner, B. D. Wilts, *Advanced Functional Materials* **2023**, *n/a* 2302720, eprint: <https://onlinelibrary.wiley.com/doi/pdf/10.1002/adfm.202302720>.

- [37] V. Bauernfeind, V. Saranathan, K. Djeghdi, E. Longo, S. Flenner, I. Greving, U. Steiner, B. D. Wilts, *Materials Today Advances* **2024**, *23*.
- [38] O. Delgado-Friedrichs, M. O’Keeffe, RCSR, **2025**, URL <http://rcsr.net/nets/>.
- [39] D. Weaire, C. O’Carroll, M. Al-Hourani, *Modern Physics Letters B* **1987**, publisher: World Scientific Publishing Company.
- [40] N. Metropolis, A. W. Rosenbluth, M. N. Rosenbluth, A. H. Teller, E. Teller, *The Journal of Chemical Physics* **1953**, *21*, 6 1087.
- [41] S. von Alftan, A. Kuronen, K. Kaski, *Physical Review B* **2003**, *68*, 7 073203, publisher: American Physical Society.
- [42] R. Gross, A. Marx, *Festkörperphysik*, Oldenbourg Wissenschaftsverlag, München, **2012**.
- [43] L. L. Whyte, *The American Mathematical Monthly* **1952**, *59*, 9 606.
- [44] P. J. Steinhardt, D. R. Nelson, M. Ronchetti, *Physical Review B* **1983**, *28*, 2 784, publisher: American Physical Society.
- [45] A. Blondel, M. Karplus, *Journal of Computational Chemistry* **1996**, *17*, 9 1132, eprint: <https://onlinelibrary.wiley.com/doi/10.1002/%28SICI%291096-987X%2819960715%2917%3A9%3C1132%3A%3AAID-JCC5%3E3.0.CO%3B2-T>.
- [46] R. I. Cukier, *The Journal of Physical Chemistry B* **2015**, *119*, 9 3621, publisher: American Chemical Society.
- [47] S. Torquato, *Physics Reports* **2018**, *745* 1, hyperuniform States of Matter.
- [48] L. D. Gelb, K. E. Gubbins, *Langmuir* **1999**, *15*, 2 305, publisher: American Chemical Society.
- [49] S. Song, Q. Ding, J. Wei, *Physical Review E* **2019**, *100*, 5 053314, publisher: American Physical Society.
- [50] M. A. Klatt, R. M. Ziff, S. Torquato, *Physical Review E* **2021**, *104*, 1 014127, publisher: American Physical Society.
- [51] S. Torquato, *Random Heterogeneous Materials: Microstructure and Macroscopic Properties*, Interdisciplinary Applied Mathematics. Springer New York, **2013**.
- [52] S. Agrawal, S. Galmarini, M. Kröger, *Physical Review E* **2023**, *107*, 1 015307, publisher: American Physical Society.
- [53] S. Torquato, F. H. Stillinger, *Phys. Rev. E* **2003**, *68* 041113.
- [54] D. Hawat, G. Gautier, R. Bardenet, R. Lachièze-Rey, *Statistics and Computing* **2023**, *33*, 3 61.
- [55] S. Torquato, *Physical Review E* **2021**, *104*, 5 054102, publisher: American Physical Society.
- [56] S. Prager, *Chemical Engineering Science* **1963**, *18*, 4 227.
- [57] K. Goetzke, H. J. Klein, *Journal of Non-Crystalline Solids* **1991**, *127*, 2 215.

[58] F. Tampieri, In D. KIRK, editor, *Graphics Gems III (IBM Version)*, 231–232. Morgan Kaufmann, San Francisco, ISBN 978-0-12-409673-8, **1992**, URL <https://www.sciencedirect.com/science/article/pii/B978008050755250052X>.

[59] J. D. Joannopoulos, S. G. Johnson, J. N. Winn, R. D. Meade, *Photonic Crystals: Molding the Flow of Light - Second Edition*, Princeton University Press, rev - revised, 2 edition, **2008**.

[60] R. K. Cersonsky, J. Antonaglia, B. D. Dice, S. C. Glotzer, *Nature Communications* **2021**, *12*, 1 2543, publisher: Nature Publishing Group.

[61] K. Michielsen, D. Stavenga, *Journal of the Royal Society, Interface / the Royal Society* **2007**, *5* 85.

[62] C. Cui, G. Wei, M. Saba, L. Han, Comprehensive enumeration of three-dimensional photonic crystals enabled through deep learning assisted fourier synthesis, **2025**, URL <http://arxiv.org/abs/2501.18495>.

[63] G. Zhang, F. H. Stillinger, S. Torquato, *Soft Matter* **2017**, *13* 6197.

[64] O. U. Uche, S. Torquato, F. H. Stillinger, *Physical Review E* **2006**, *74*, 3 031104, publisher: American Physical Society.

[65] A. Paszke, S. Gross, F. Massa, A. Lerer, J. Bradbury, G. Chanan, T. Killeen, Z. Lin, N. Gimelshein, L. Antiga, A. Desmaison, A. Kopf, E. Yang, Z. DeVito, M. Raison, A. Tejani, S. Chilamkurthy, B. Steiner, L. Fang, J. Bai, S. Chintala, In H. Wallach, H. Larochelle, A. Beygelzimer, F. d'Alché-Buc, E. Fox, R. Garnett, editors, *Advances in Neural Information Processing Systems*, volume 32. Curran Associates, Inc., **2019** URL https://proceedings.neurips.cc/paper_files/paper/2019/file/bdbca288fee7f92f2bfa9f7012727740-Paper.pdf.

[66] I. Jolliffe, *Principal Component Analysis*, Springer Series in Statistics. Springer, **2002**.

[67] C. Schittenkopf, G. Deco, W. Brauer, *Neural Networks* **1997**, *10*, 3 505.

[68] M. E. Tipping, C. M. Bishop, *Journal of the Royal Statistical Society Series B: Statistical Methodology* **2002**, *61*, 3 611.

[69] Pytorch documentation, URL <https://pytorch.org/docs/stable/index.html>.

[70] A. J. Hughes, D. E. Grawoig, *Statistics: A Foundation for Analysis*, 344–345, Addison-Wesley Publishing Company, Reading, Mass., ISBN 0201030217, **1971**.

[71] L. S. Froufe-Pérez, M. Engel, P. F. Damasceno, N. Muller, J. Haberko, S. C. Glotzer, F. Scheffold, *Physical Review Letters* **2016**, *117*, 5 053902.

[72] L. Dal Negro, R. Wang, F. A. Pinheiro, *Crystals* **2016**, *6*, 12 161, number: 12.

[73] S. Yu, C.-W. Qiu, Y. Chong, S. Torquato, N. Park, *Nature Reviews Materials* **2020**, *6*, 3 226.

[74] R. Sapienza, *Nature Physics* **2022**, *18*, 9 976.

[75] F. Hemmann, Computer-generation of disordered networks with targeted structural properties, **2026**, URL <https://doi.org/10.5281/zenodo.17979317>.

[76] F. Hemmann, V. Glauser, M. Saba, NCCR Bio-Inspired Materials, Disordered network generation and analysis, **2026**, URL <https://github.com/florinhem/disordered-network-gen-analysis>.

Appendices

A List of order metrics

Order metric		Meaning
Network primitives	σ_r	Bond length standard deviation
	σ_θ	Bond angle standard deviation
	\bar{q}_l for all $l \in \{0, 1, \dots, 12\}$	Mean Steinhardt local bond order parameter
	σ_{q_l} for all $l \in \{0, 1, \dots, 12\}$	Steinhardt local bond order parameter standard deviation
Homogeneity	h_ϕ	Dihedral angle entropy
	r_c	Coordinated neighbor distance
	r_u	Uncoordinated neighbor distance
	δ_c	Critical pore radius
Isotropy	α	Hyperuniformity metric
	h_b	Bond orientation entropy
	A_v	Vertex anisotropy metric
	A_b	Bond anisotropy metric
Topology	\bar{Z}	Mean coordination number
	σ_Z	Coordination number standard deviation
	\bar{s}	Mean ring size
	σ_s	Ring size standard deviation
	\bar{r}_s	Mean ring radius
	σ_{r_s}	Ring radius standard deviation

Table 2: A complete list of all order metrics for spatial networks defined in Section 3.

B Effect of input parameters of the extended WWW algorithm

In the main article, we analyze how the input parameters of the extended WWW algorithm affect the networks from the initial crystalline **ctn** network. In this section, we provide an analogue investigation of networks generated from the five other initial networks introduced in the main text, Section 4.1: **bcu_{mod}**, **pcu_{mod}**, **dia**, **srs**, and **lcs**.

B.1 $\mathbf{bcu}_{\text{mod}}$

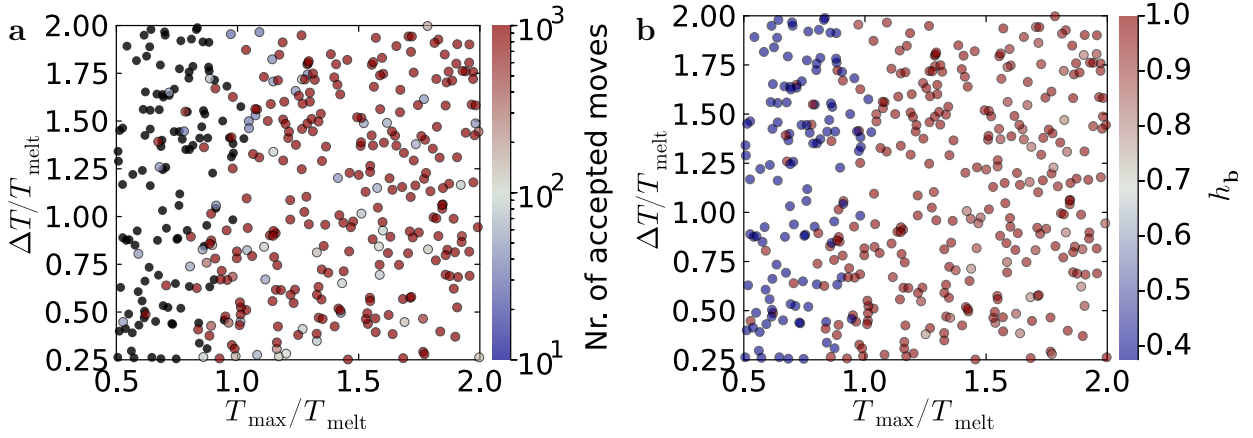


Figure 19: Illustration of the melting transition for networks generated from the initial $\mathbf{bcu}_{\text{mod}}$. **a** The number of accepted Monte Carlo moves plotted against T_{max} and ΔT . Black markers correspond to networks with 10 or fewer accepted moves. **b** Bond orientation entropy h_b .

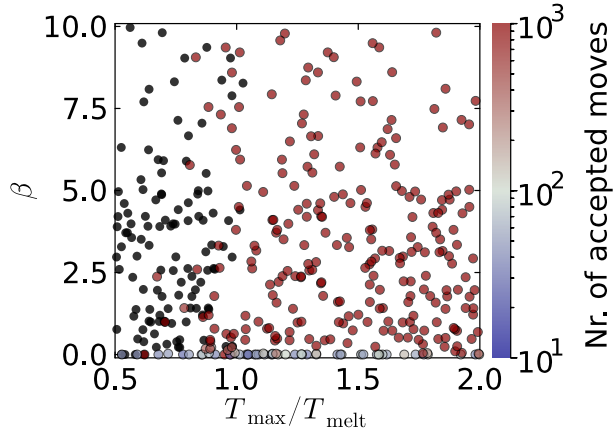


Figure 20: The number of accepted Monte Carlo moves for the initial $\mathbf{bcu}_{\text{mod}}$ plotted against T_{max} and ΔT . Black markers correspond to networks with 10 or fewer accepted moves.

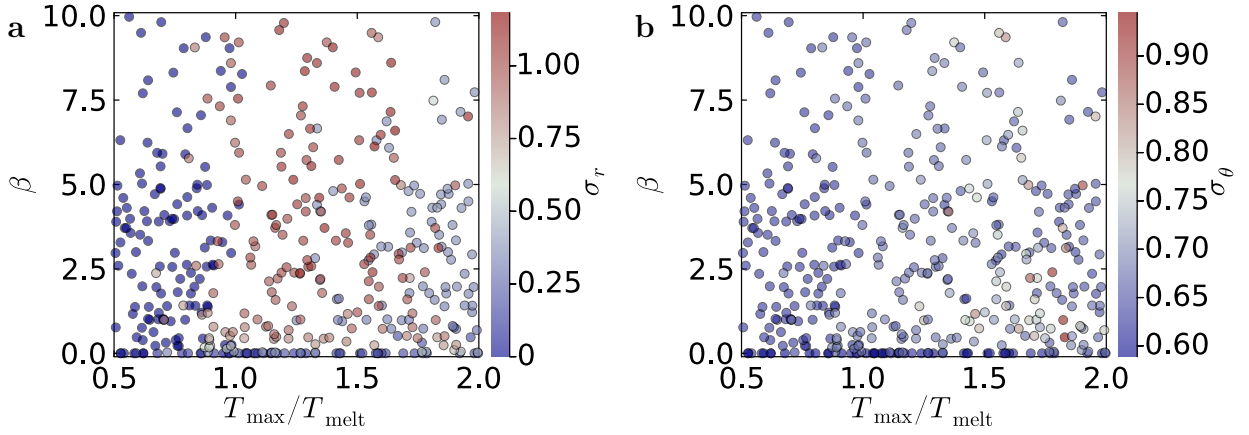


Figure 21: The network primitive metrics for networks generated from the initial $\mathbf{bcu}_{\text{mod}}$ are plotted against the algorithm inputs T_{max} and β . Red colors indicate high disorder with respect to the corresponding metric. **a** Bond length standard deviation σ_r . **b** Bond angle standard deviation σ_θ .

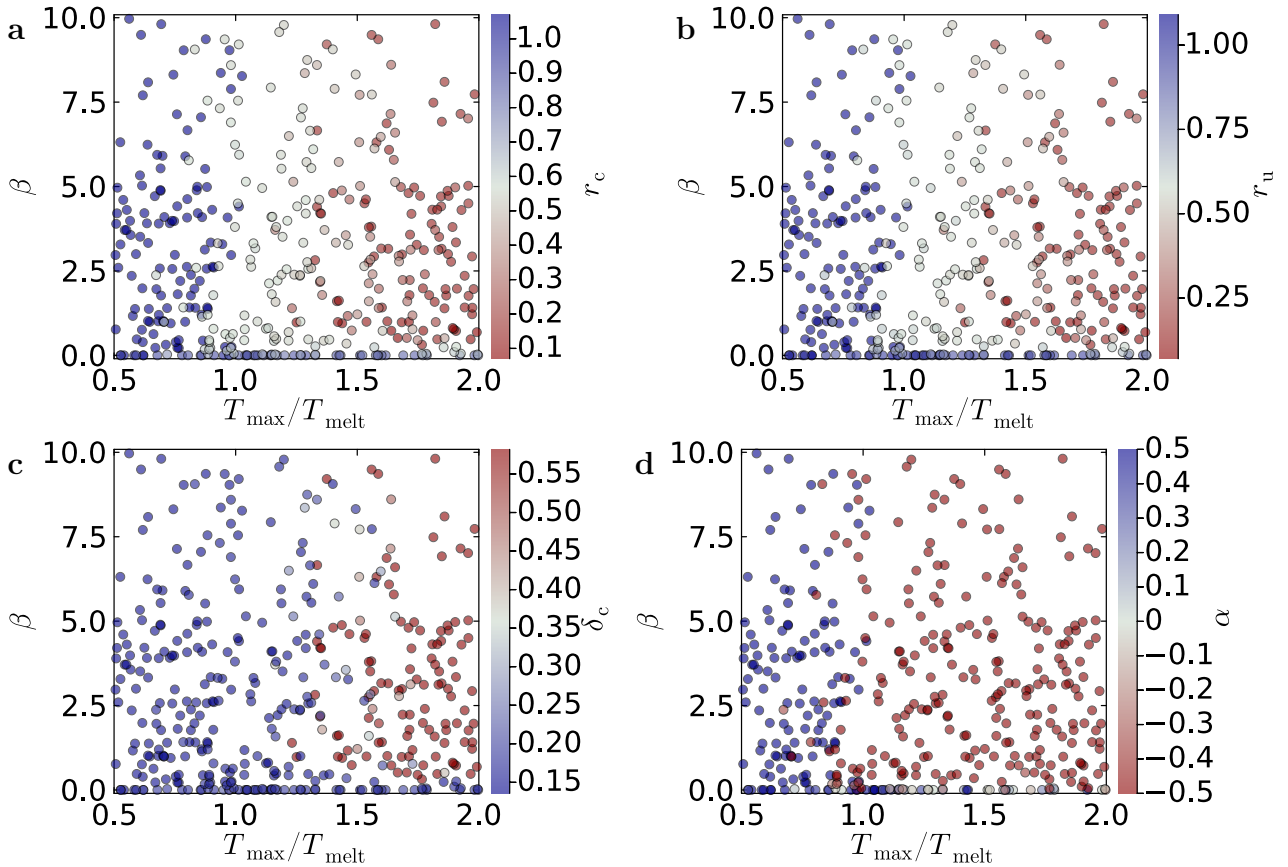


Figure 22: The homogeneity metrics for networks generated from the initial $\mathbf{bcu}_{\text{mod}}$ are plotted against the algorithm inputs T_{max} and β . Red colors indicate high disorder with respect to the corresponding metric. **a** Coordinated neighbor distance r_c . **b** Uncoordinated neighbor distance r_u . **c** Critical pore radius δ_c . **d** Hyperuniformity metric α .

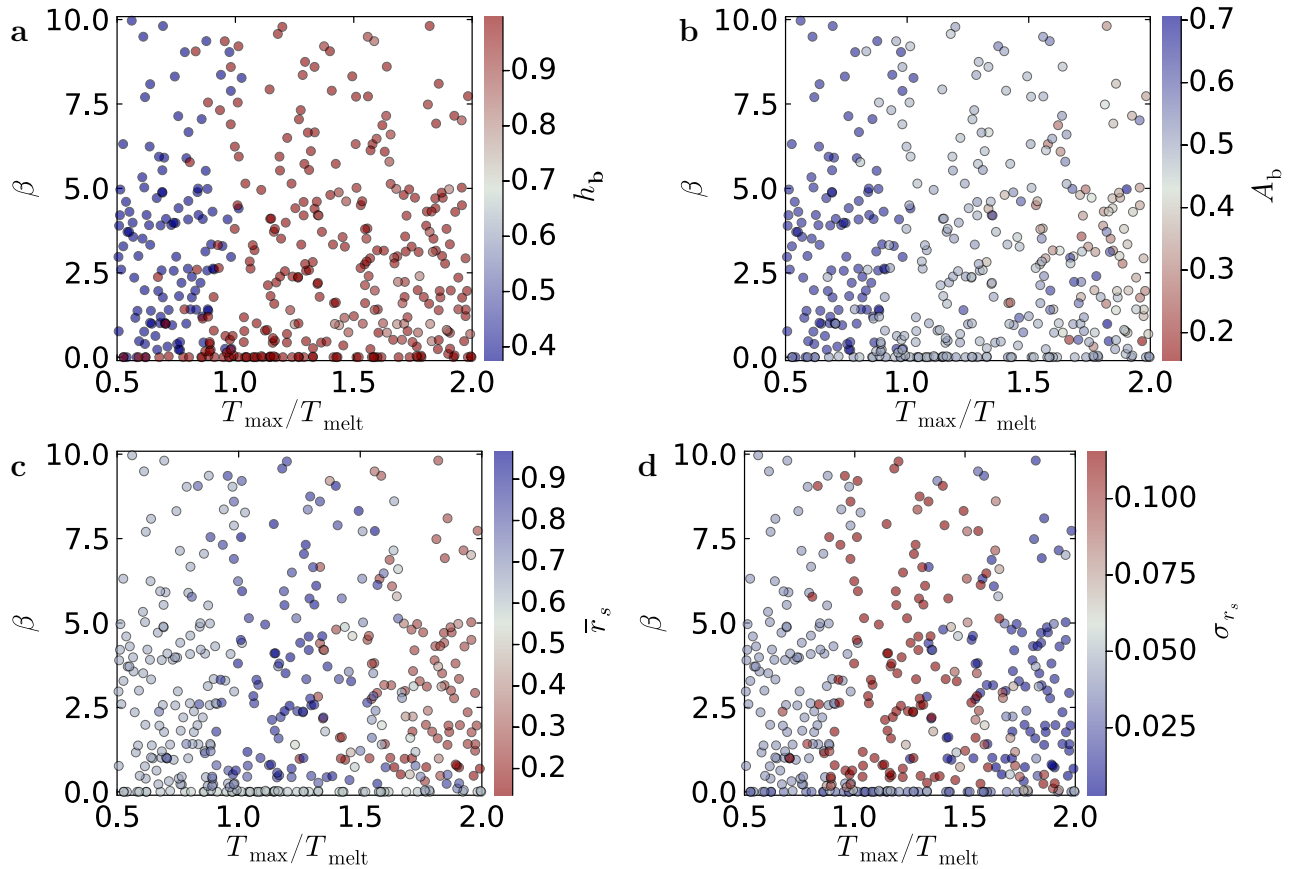


Figure 23: The isotropy and topology metrics for networks generated from the initial bcu_{mod} as a function of the network generation algorithm inputs T_{\max} and β . Red colors indicate high disorder with respect to the corresponding metric. **a** Bond orientation entropy h_b . **b** Structure factor anisotropy metric A_b . **c** Mean ring radius \bar{r}_s . **d** Ring radius standard deviation σ_{r_s} .

B.2 pcu_{mod}

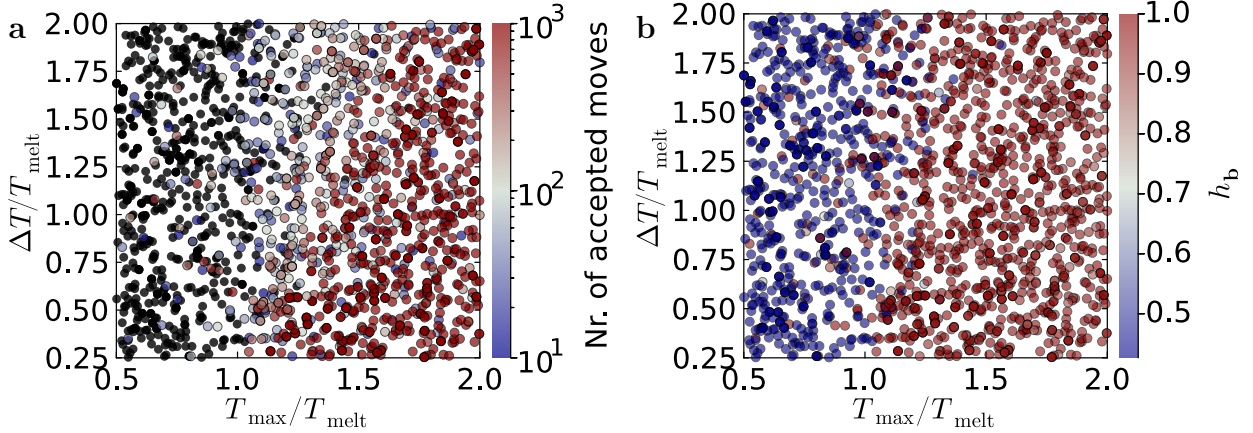


Figure 24: Illustration of the melting transition for networks generated from the initial pcu_{mod} . **a** The number of accepted Monte Carlo moves plotted against T_{\max} and ΔT . Black markers correspond to networks with 10 or fewer accepted moves. **b** Bond orientation entropy h_b .

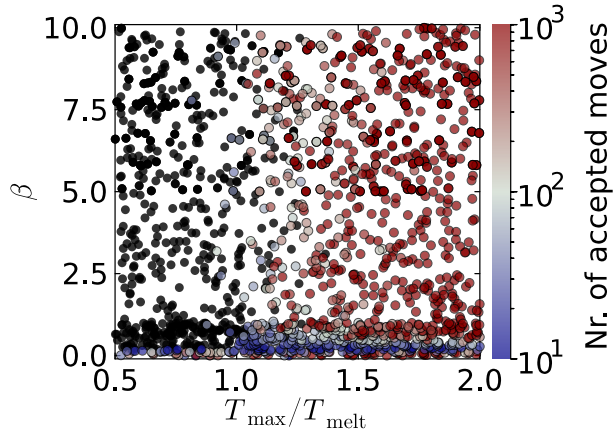


Figure 25: The number of accepted Monte Carlo moves for the initial pcu_{mod} plotted against T_{\max} and ΔT . Black markers correspond to networks with 10 or fewer accepted moves.

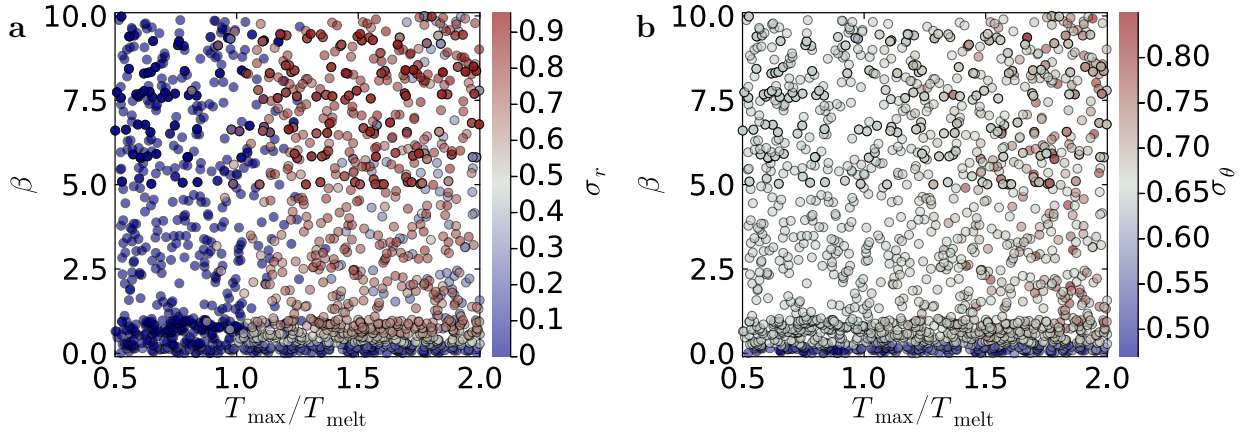


Figure 26: The network primitive metrics for networks generated from the initial $\mathbf{pcu}_{\text{mod}}$ are plotted against the algorithm inputs T_{max} and β . Red colors indicate high disorder with respect to the corresponding metric. **a** Bond length standard deviation σ_r . **b** Bond angle standard deviation σ_θ .

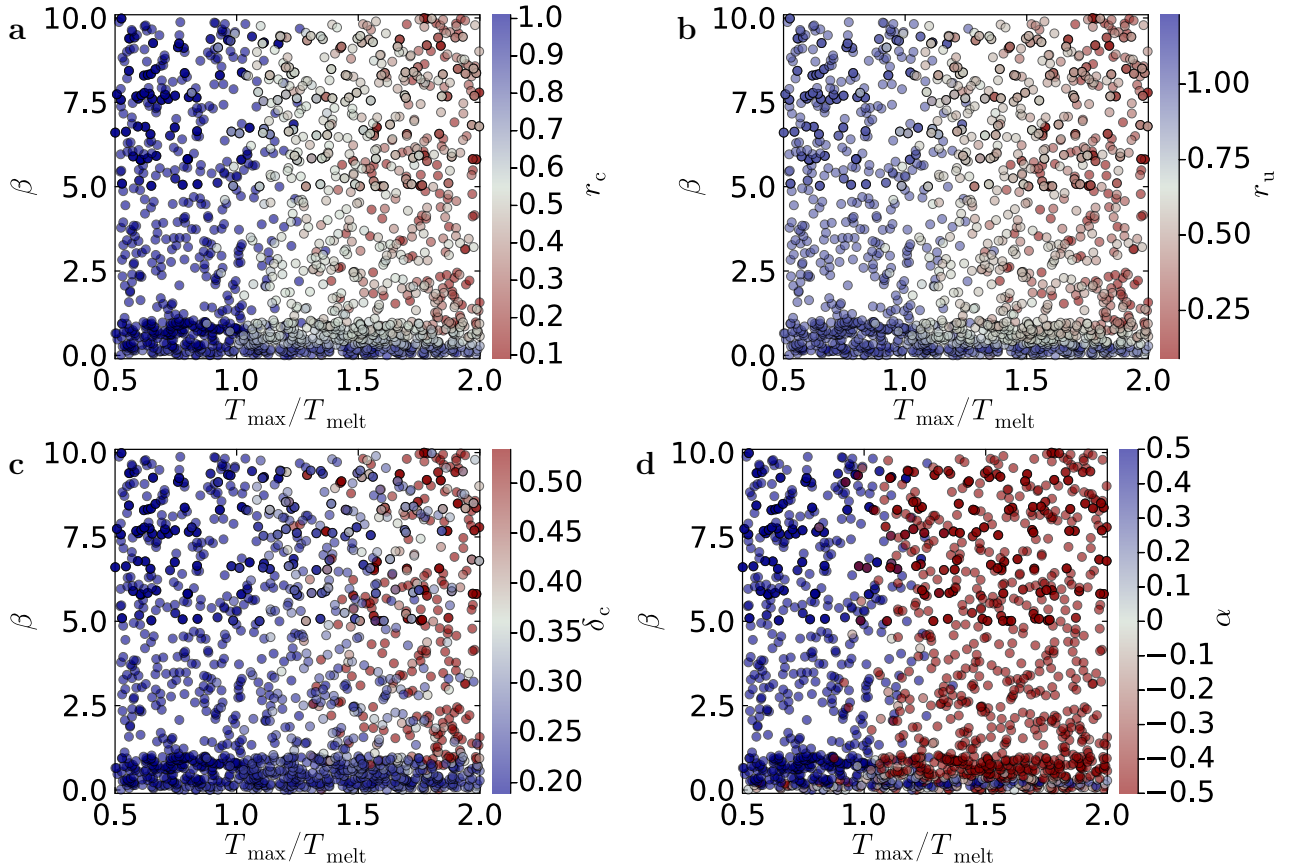


Figure 27: The homogeneity metrics for networks generated from the initial $\mathbf{pcu}_{\text{mod}}$ are plotted against the algorithm inputs T_{max} and β . Red colors indicate high disorder with respect to the corresponding metric. **a** Coordinated neighbor distance r_c . **b** Uncoordinated neighbor distance r_u . **c** Critical pore radius δ_c . **d** Hyperuniformity metric α .

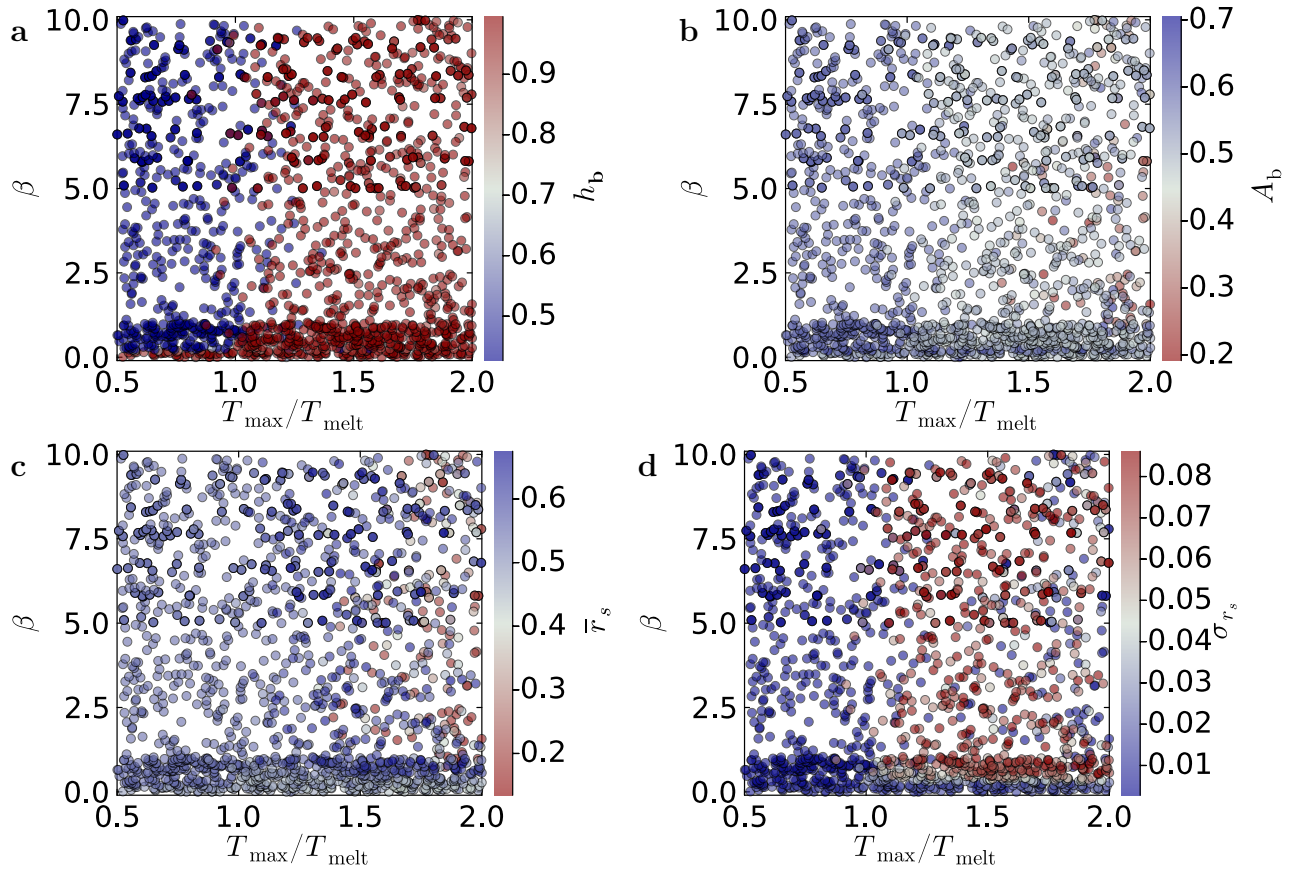


Figure 28: The isotropy and topology metrics for networks generated from the initial pcu_{mod} as a function of the network generation algorithm inputs T_{\max} and β . Red colors indicate high disorder with respect to the corresponding metric. **a** Bond orientation entropy h_b . **b** Structure factor anisotropy metric A_b . **c** Mean ring radius \bar{r}_s . **d** Ring radius standard deviation σ_{r_s} .

B.3 dia

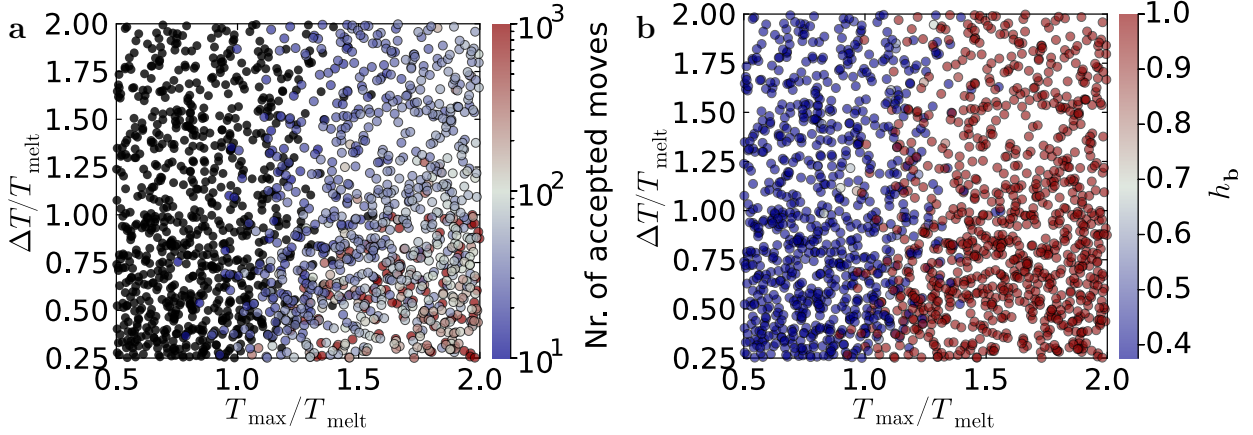


Figure 29: Illustration of the melting transition for networks generated from the initial **dia**. **a** The number of accepted Monte Carlo moves plotted against T_{\max} and ΔT . Black markers correspond to networks with 10 or fewer accepted moves. **b** Bond orientation entropy h_b .

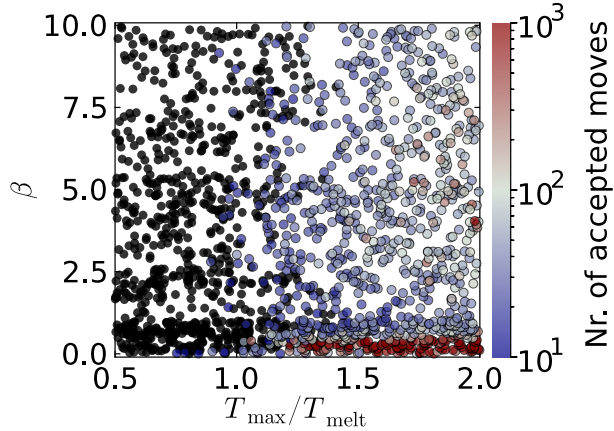


Figure 30: The number of accepted Monte Carlo moves for the initial **dia** plotted against T_{\max} and ΔT . Black markers correspond to networks with 10 or fewer accepted moves.

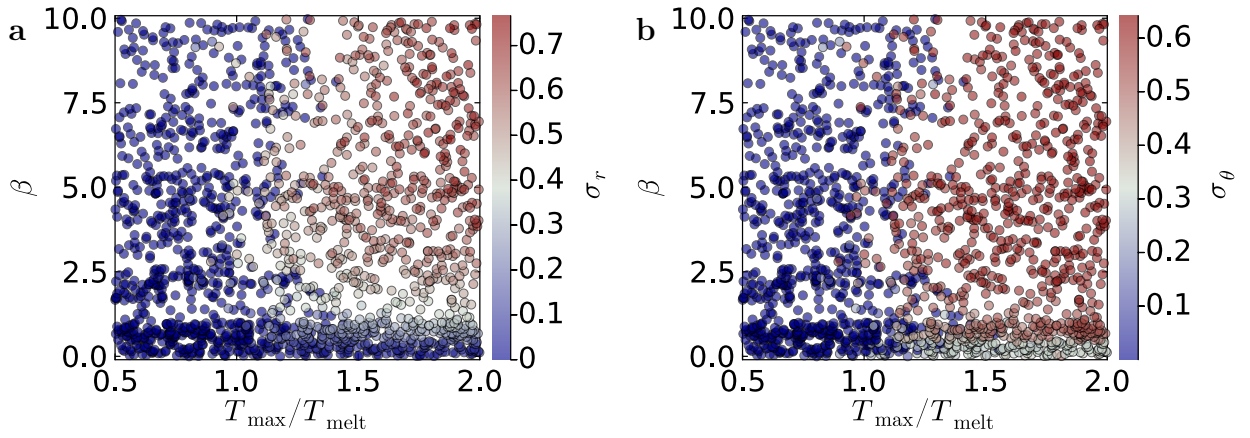


Figure 31: The network primitive metrics for networks generated from the initial **dia** are plotted against the algorithm inputs T_{\max} and β . Red colors indicate high disorder with respect to the corresponding metric. **a** Bond length standard deviation σ_r . **b** Bond angle standard deviation σ_θ .

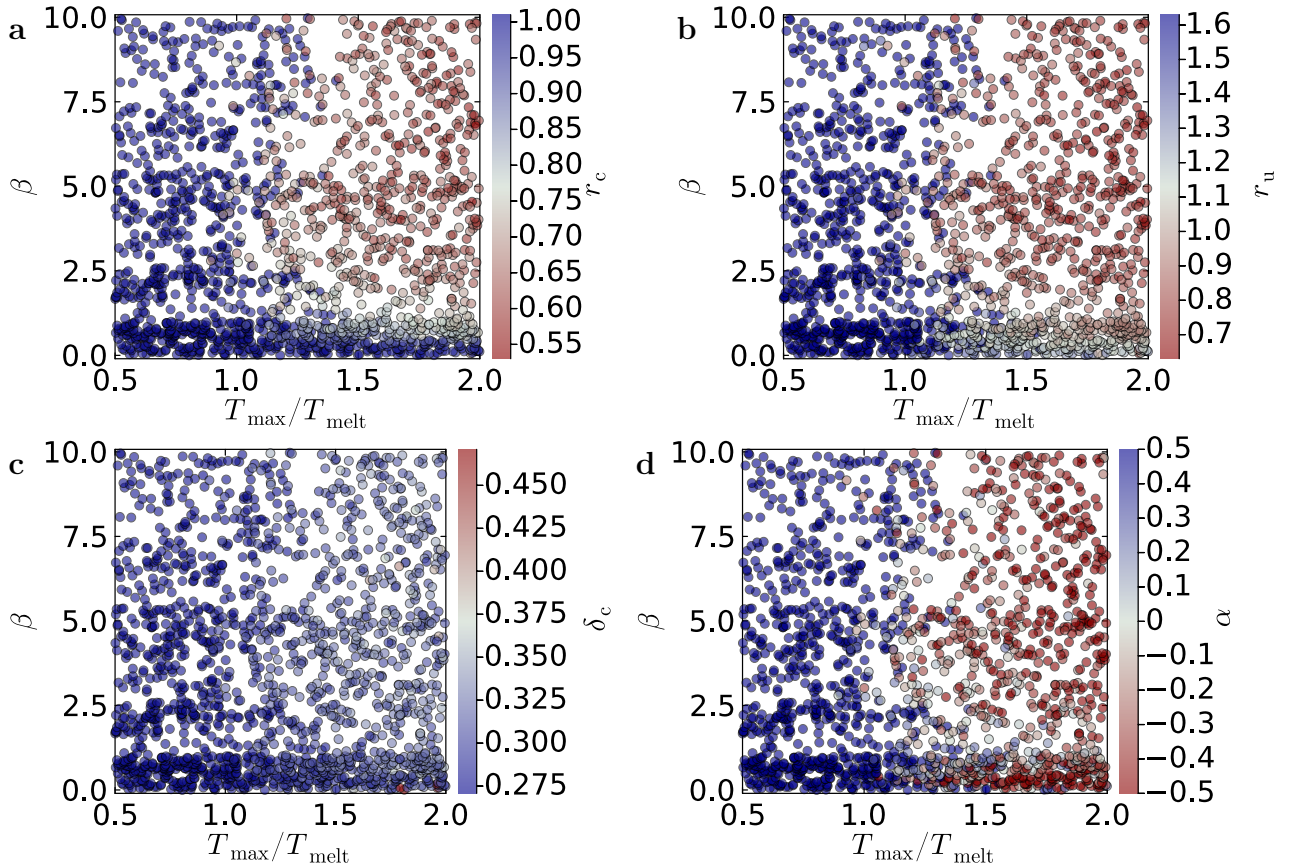


Figure 32: The homogeneity metrics for networks generated from the initial **dia** are plotted against the algorithm inputs T_{\max} and β . Red colors indicate high disorder with respect to the corresponding metric. **a** Coordinated neighbor distance r_c . **b** Uncoordinated neighbor distance r_u . **c** Critical pore radius δ_c . **d** Hyperuniformity metric α .

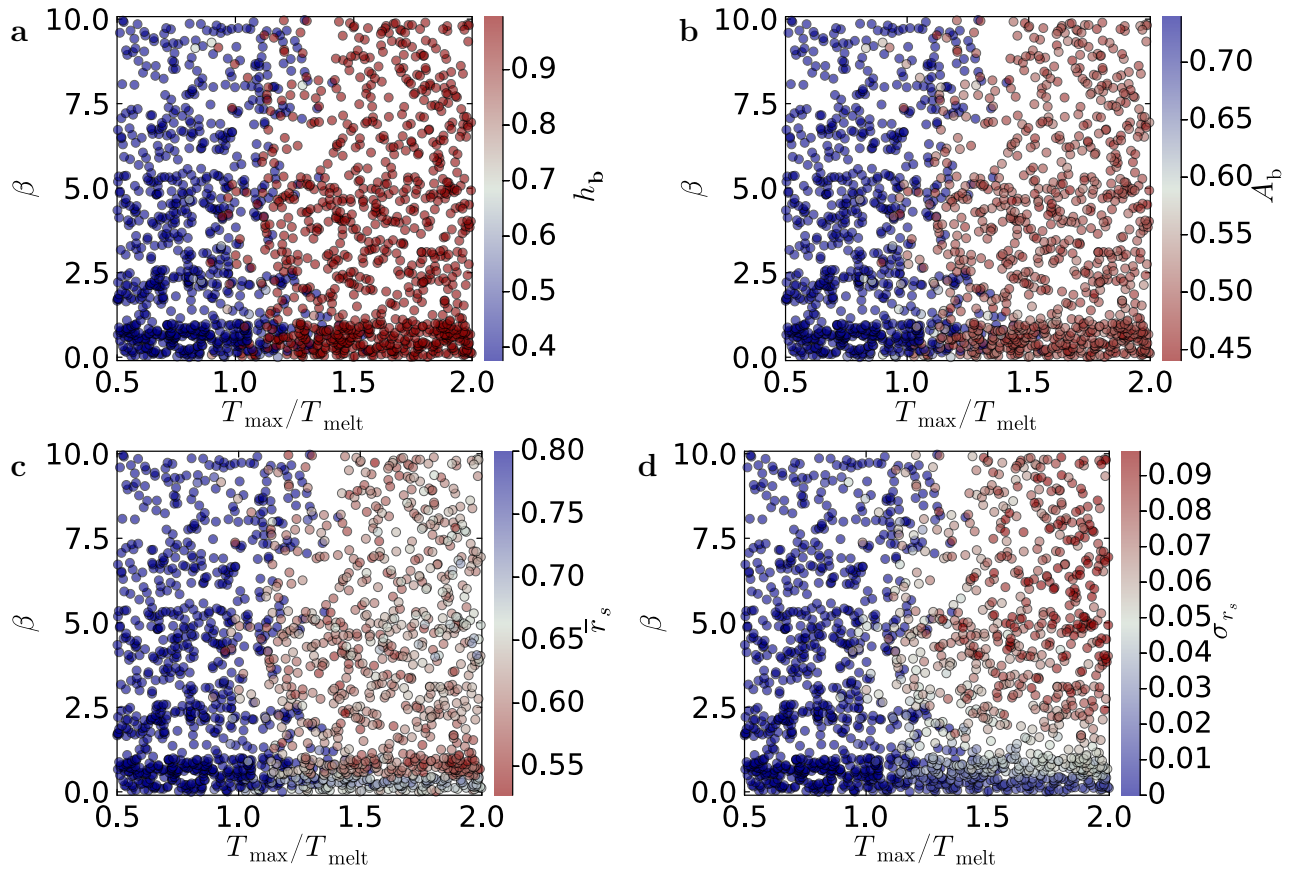


Figure 33: The isotropy and topology metrics for networks generated from the initial **dia** as a function of the network generation algorithm inputs T_{\max} and β . Red colors indicate high disorder with respect to the corresponding metric. **a** Bond orientation entropy h_b . **b** Structure factor anisotropy metric A_b . **c** Mean ring radius \bar{r}_s . **d** Ring radius standard deviation σ_{r_s} .

B.4 srs

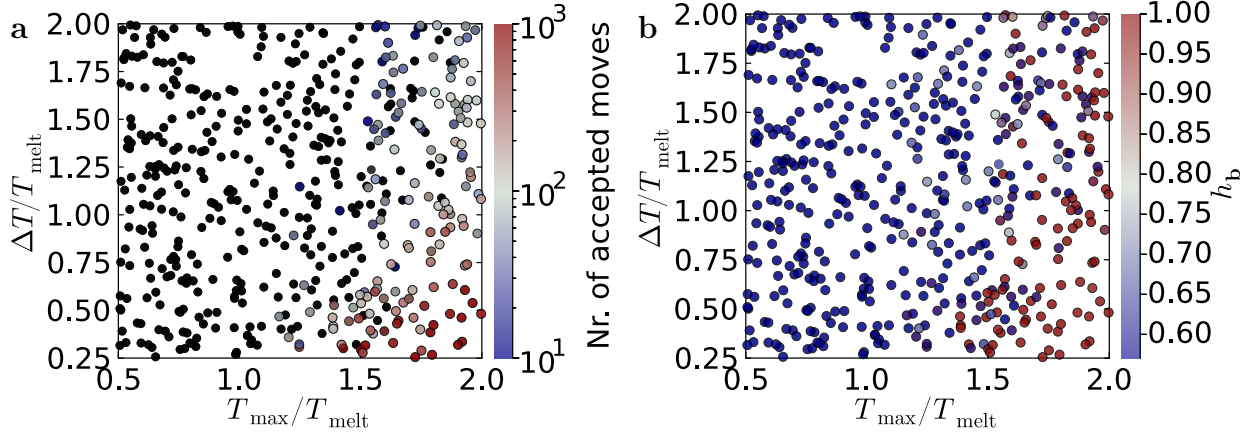


Figure 34: Illustration of the melting transition for networks generated from the initial **srs**. **a** The number of accepted Monte Carlo moves plotted against T_{\max} and ΔT . Black markers correspond to networks with 10 or fewer accepted moves. **b** Bond orientation entropy h_b .

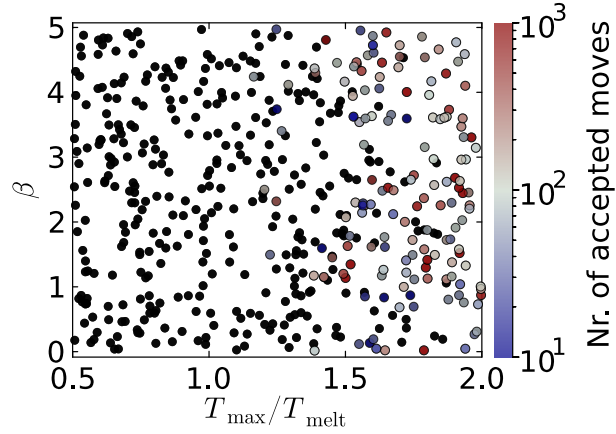


Figure 35: The number of accepted Monte Carlo moves for the initial **srs** plotted against T_{\max} and ΔT . Black markers correspond to networks with 10 or fewer accepted moves.

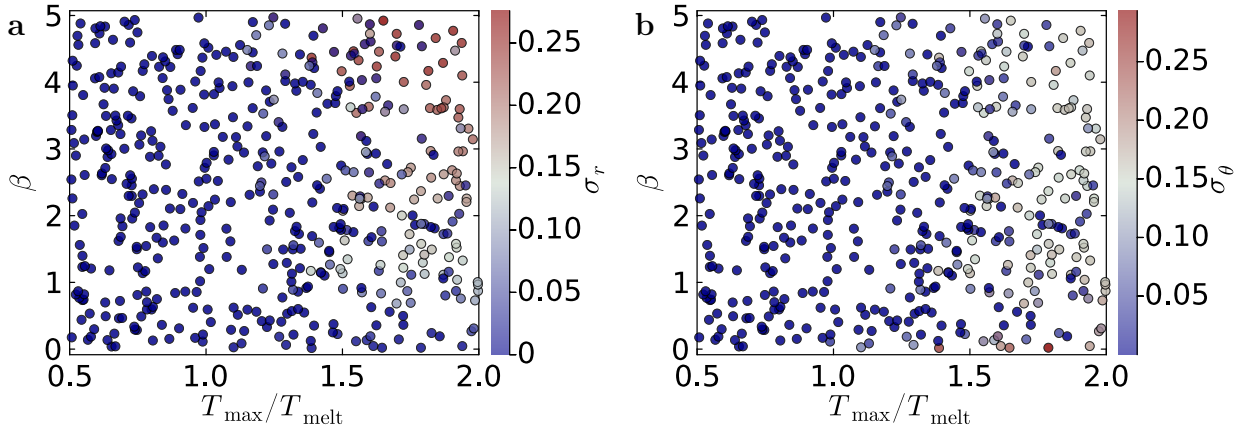


Figure 36: The network primitive metrics for networks generated from the initial **srs** are plotted against the algorithm inputs T_{\max} and β . Red colors indicate high disorder with respect to the corresponding metric. **a** Bond length standard deviation σ_r . **b** Bond angle standard deviation σ_θ .

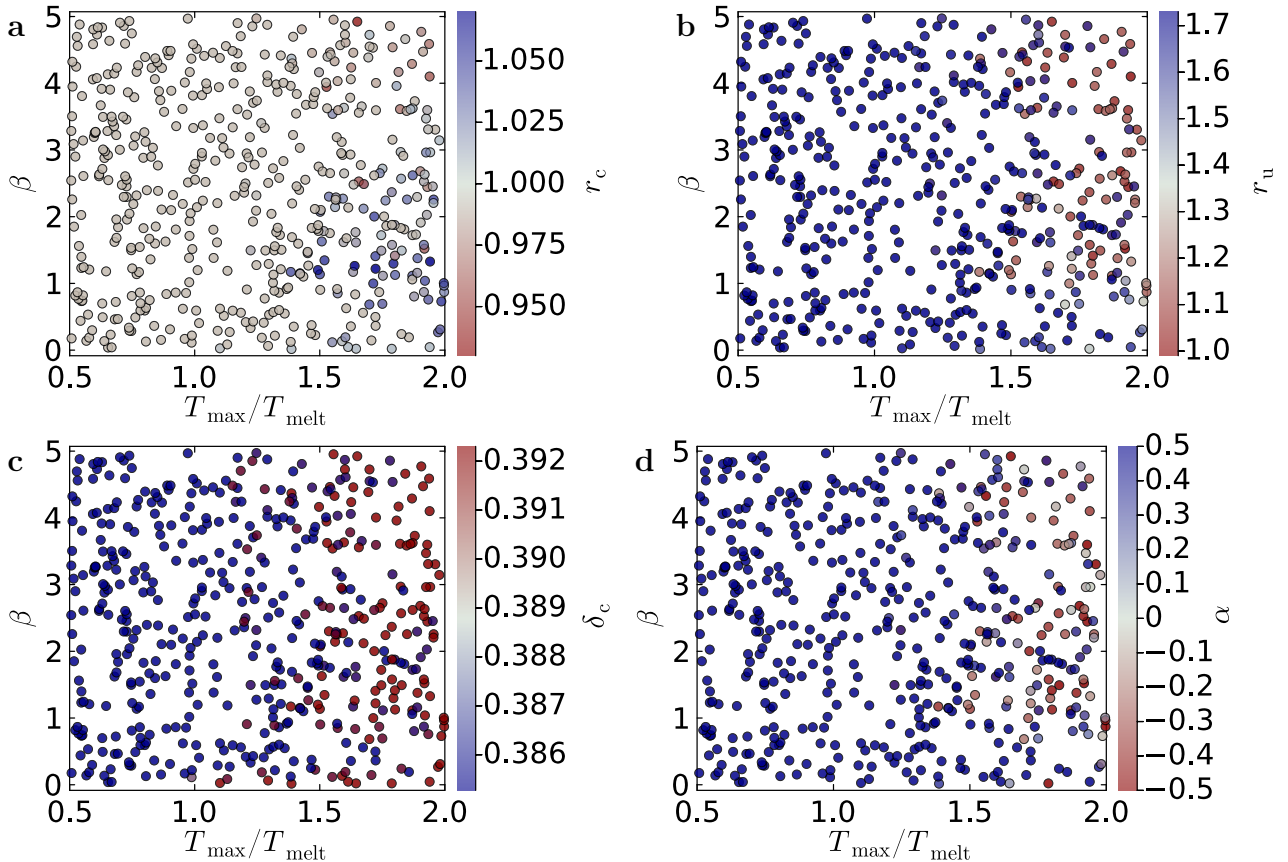


Figure 37: The homogeneity metrics for networks generated from the initial **srs** are plotted against the algorithm inputs T_{\max} and β . Red colors indicate high disorder with respect to the corresponding metric. **a** Coordinated neighbor distance r_c . **b** Uncoordinated neighbor distance r_u . **c** Critical pore radius δ_c . **d** Hyperuniformity metric α .

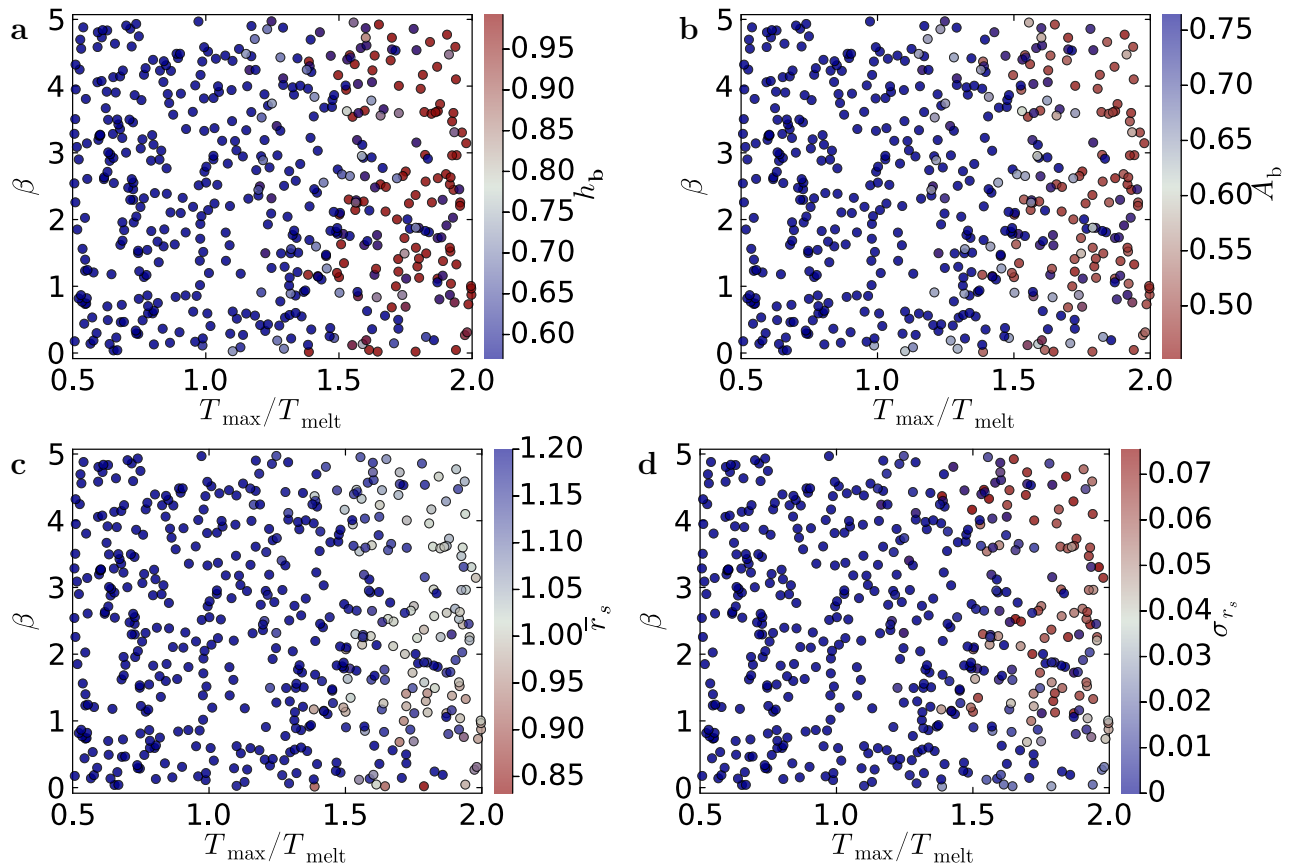


Figure 38: The isotropy and topology metrics for networks generated from the initial **srs** as a function of the network generation algorithm inputs T_{\max} and β . Red colors indicate high disorder with respect to the corresponding metric. **a** Bond orientation entropy h_b . **b** Structure factor anisotropy metric A_b . **c** Mean ring radius \bar{r}_s . **d** Ring radius standard deviation σ_{r_s} .

B.5 lcs

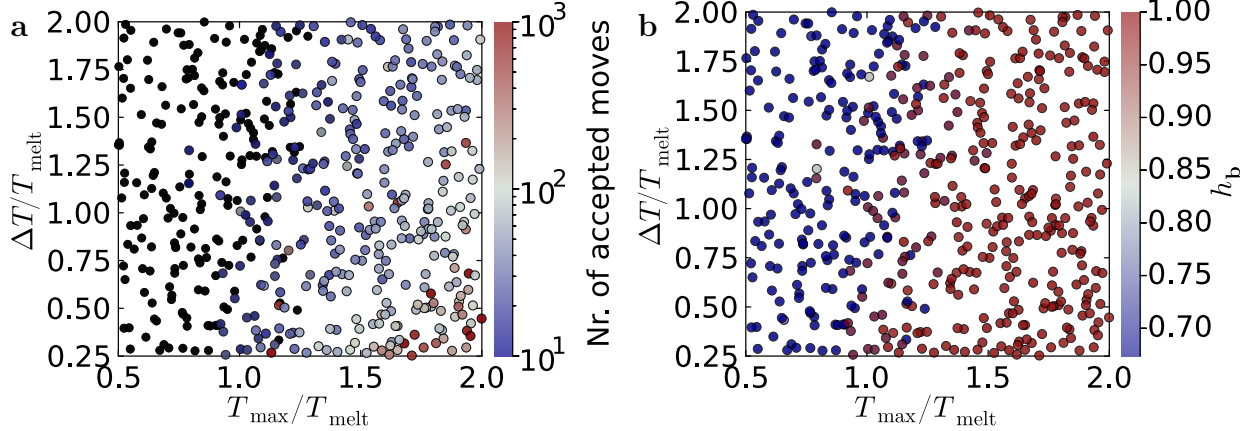


Figure 39: Illustration of the melting transition for networks generated from the initial **lcs**. **a** The number of accepted Monte Carlo moves plotted against T_{\max} and ΔT . Black markers correspond to networks with 10 or fewer accepted moves. **b** Bond orientation entropy h_b .

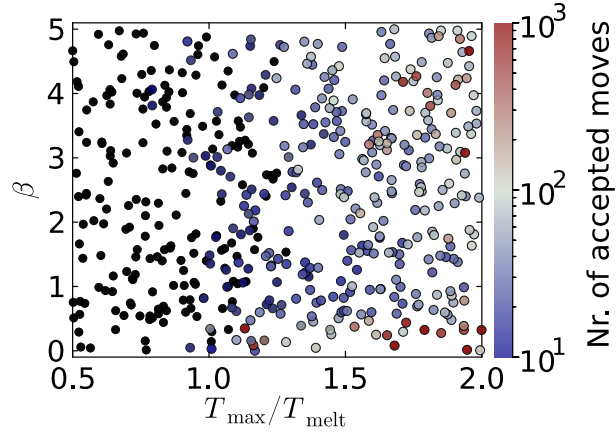


Figure 40: The number of accepted Monte Carlo moves for the initial **lcs** plotted against T_{\max} and ΔT . Black markers correspond to networks with 10 or fewer accepted moves.

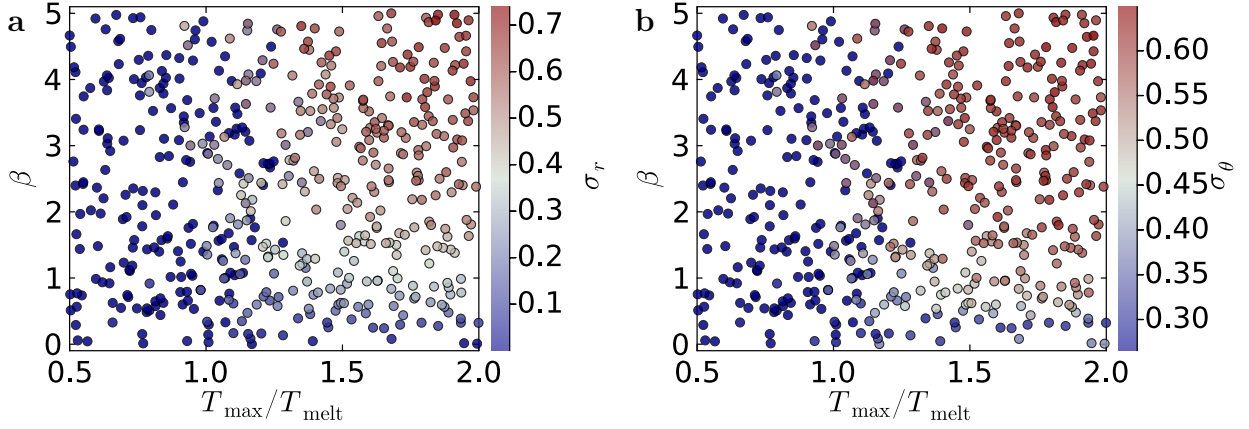


Figure 41: The network primitive metrics for networks generated from the initial **lcs** are plotted against the algorithm inputs T_{\max} and β . Red colors indicate high disorder with respect to the corresponding metric. **a** Bond length standard deviation σ_r . **b** Bond angle standard deviation σ_θ .

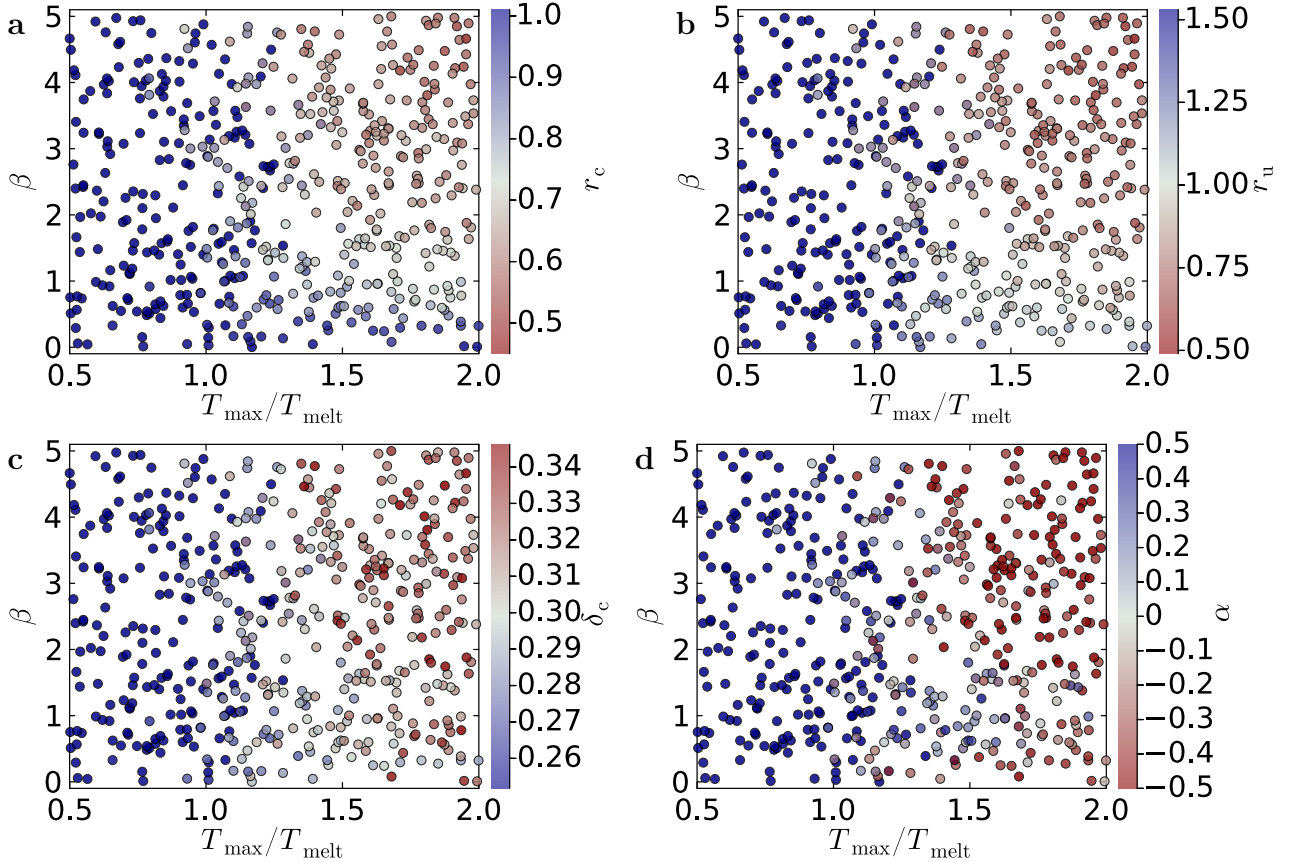


Figure 42: The homogeneity metrics for networks generated from the initial **lcs** are plotted against the algorithm inputs T_{\max} and β . Red colors indicate high disorder with respect to the corresponding metric. **a** Coordinated neighbor distance r_c . **b** Uncoordinated neighbor distance r_u . **c** Critical pore radius δ_c . **d** Hyperuniformity metric α .

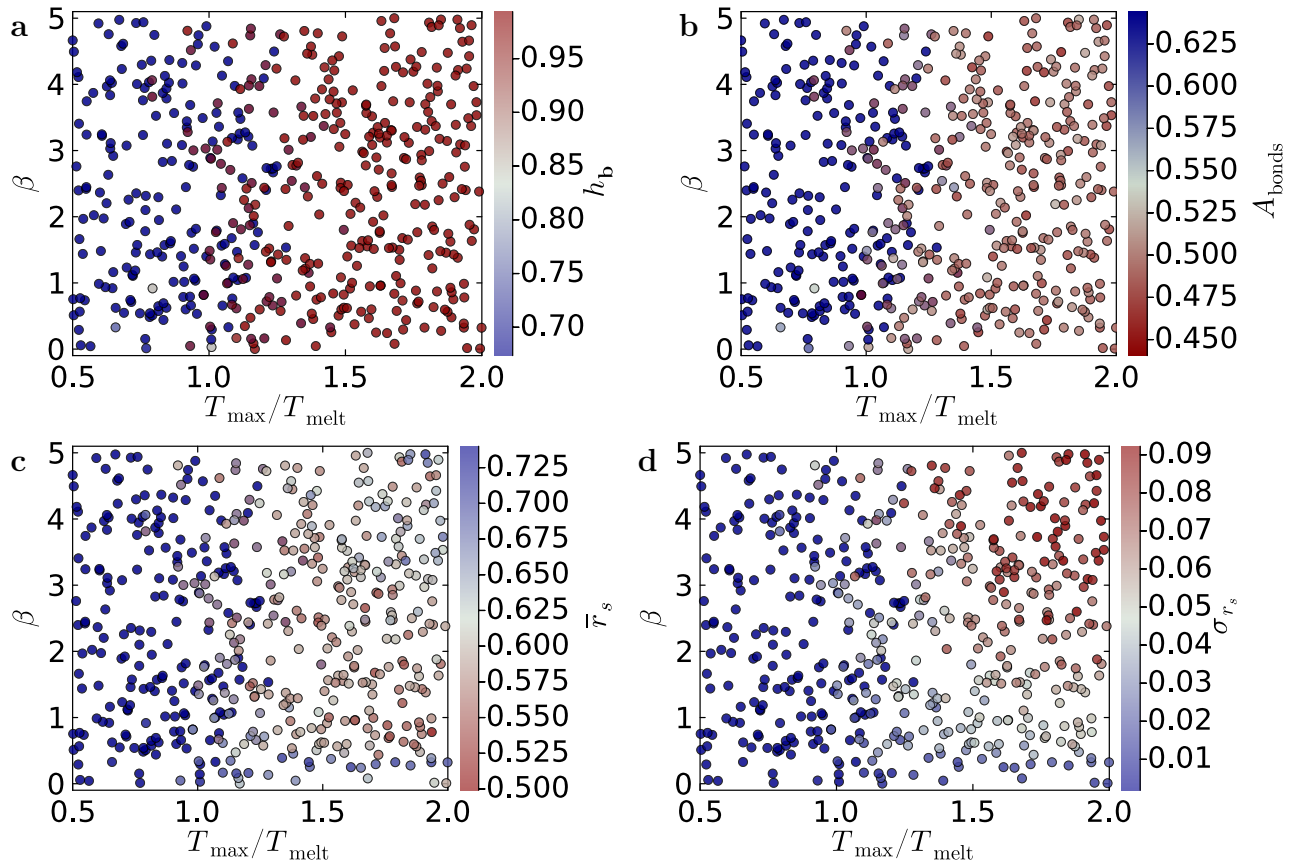


Figure 43: The isotropy and topology metrics for networks generated from the initial **lcs** as a function of the network generation algorithm inputs T_{\max} and β . Red colors indicate high disorder with respect to the corresponding metric. **a** Bond orientation entropy h_b . **b** Structure factor anisotropy metric A_b . **c** Mean ring radius \bar{r}_s . **d** Ring radius standard deviation σ_{r_s} .

C Principal component analysis of generated order metrics

Here, we provide additional information about the principal component analysis that we apply to the order metric data of networks generated from the **ctn** network (main text, Section 4.3).

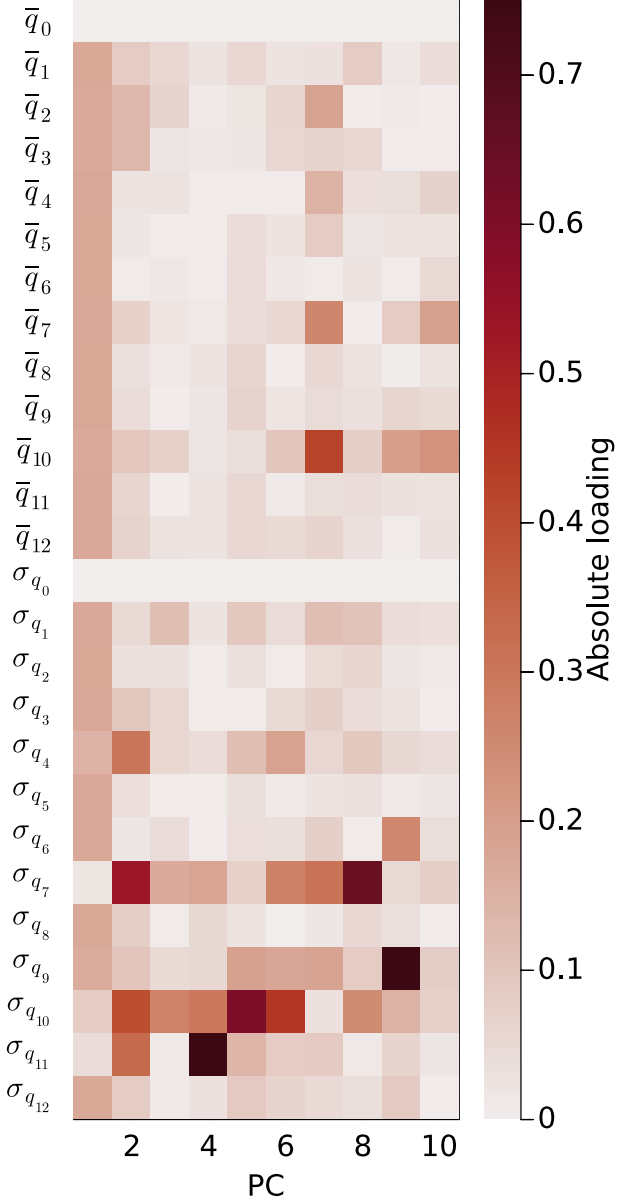


Figure 44: Absolute values of the PCA loadings with the mean Steinhardt local bond order parameters \bar{q}_l and their standard deviations σ_{q_l} . This illustration depicts the contributions of the combined loadings $\bar{\mathbf{q}}$ and $\sigma_{\mathbf{q}}$ in Figure 11b.